EFFECT OF BEAM DIFFRACTION ON NONLINEAR RAYLEIGH SURFACE WAVE MEASUREMENT

A Thesis
Presented to
The Academic Faculty

by

Chi-Luen Huang

In Partial Fulfillment
of the Requirements for the Degree
Master of Science in
Engineering Science and Mechanics

School of Civil and Environmental Engineering
Georgia Institute of Technology
May 2013

EFFECT OF BEAM DIFFRACTION ON NONLINEAR RAYLEIGH SURFACE WAVE MEASUREMENT

Approved by:

Dr. Laurence J. Jacobs, Advisor
School of Civil and Environmental Engineering
Georgia Institute of Technology

Dr. Jin-Yeon Kim
School of Civil and Environmental Engineering
Georgia Institute of Technology

Dr. Jianmin Qu
George W. Woodruff School of Mechanical Engineering
Georgia Institute of Technology

Date Approved: January 11, 2013

ACKNOWLEDGEMENTS

This thesis would never come true without the many people's helps and supports. My first gratitude is dedicated to my adviser Dr. Jacobs. He led me into the area of wave propagation, and it was him who gave me an opportunity to study and to do this research. His guidance and supports always encouraged me on my way of research. I would also like to take this opportunity to express my appreciation to Dr. Kim. He always gave me ideas whenever I was stuck, and always inspired me with his precious knowledge. In private, I enjoyed every causal chat with him, especially for those topics about history. I also want to thank Dr. Qu for his granting to be one of my thesis committee members. My gratitude also goes to my laboratory fellows Christian, Johann, Daniel, and Katie. It was what a pleasure to work with them in the same library. Johann and Christian always were always able to figure out ways to bring joy into the Lab, and they cheered me up whenever I felt down. Daniel and I shared so many topics about cars and travels, and it seemed like I can always find wisdom on him. Katie is a really knowledgeable person, and she was always willing to give me instructions of experiment setup and answer my tiny questions about experiments. Most importantly, the Donuts Wednesday with you all fellows in the Lab will be the most special and precious memory in my mind forever. My last but the most gratitude goes to my parents. It was their supports, mentally and financially, to make my degree and my life in the US all possible, and you always understand my struggles about life.

TABLE OF CONTENTS

LIST OF TABLES

LIST OF FIGURES

LIST OF SYMBOLS AND ABBREVIATIONS

Symbol	Description
A_1'	Amplitude of the fundamental harmonic frequency
A_2'	Amplitude of the second harmonic
β	Nonlinearity parameter
ω	Angular frequency
c	Wave phase velocity
c_l, c_t, c_R	Longitudinal, transverse, and Rayleigh wave phase velocity
f	Frequency
k	Wavenumber
λ	Wavelength
C_{ijkl}	Fourth order stiffness tensor
n_i	Normal vector
t_i	Traction
ε_{ij}	Strain tensor
σ_{ij}	Stress tensor
ρ	Density
ν	Poisson's ratio
λ, μ	Lamé constants
$\varphi, \boldsymbol{\psi}$	Displacement potentials
∇	Nabla operator
FFT	Fast Fourier transform

SUMMARY

This research investigates the effects of beam diffraction from a source of finite width on nonlinear Rayleigh wave propagation in an elastic half space. Existing quasi-linear models accounting for diffraction effect on nonlinear Rayleigh waves are studied, implemented, and compared. Measurements are conducted on a specimen of 7075-T651 aluminum. In the measurements, tone burst signals are generated, converted into Rayleigh waves in the specimen, and detected with the use of Plexiglas wedges. The nonlinear Rayleigh waves collected at different propagation distances are analyzed with fast Fourier transform in order to calculate the normalized second harmonic amplitudes. A method is developed to reduce the range of the measurement distance by compensating diffraction effect in the near field. Those quasi-linear theoretical models are employed in a combination with the proposed method, and the computation results are compared with experiment ones. Finally, feasibilities of the proposed method with different models employed are compared in the results of normalized second harmonic amplitude vs propagation distance.

CHAPTER 1

INTRODUCTION

1.1 Motivation and Objective

Previous work [4] [11] [19]has shown that nonlinear ultrasonic Rayleigh waves can be used to evaluate material damage due to plastic deformation and fatigue. In this measurement, a relatively small wedge transducer is employed to launch Rayleigh surface waves in the specimen and the first and second harmonic amplitudes are measured in the farfield as a function of propagation distance. In order to obtain a reliable set of measurement data, one needs to make numerous points in a wide range of distance, which can be impractical in many cases. The objective of this research is to develop a method to reduce the required range of measurement distance so as to enhance the applicability of the characterization method by using nonlinear Rayleigh waves to practical uses.

7075-T651 aluminum is a commonly used material for essential structural parts including aircraft gears, bike frames, and all terrain vehicle (ATV) sprockets. Sometimes those parts could be small in dimension or located at narrow places, and thus there is a difficulty for the measurements mentioned above to perform on. Therefore, this material is chosen for the specimen in this research.

1.2 Literature Review

Nonlinear acoustic waves have been investigated, and been widely applied to areas such as medical, sonar, and nondestructive evaluation for a long time. In these areas intense directional sound beams are employed, but a good model for their propagation in real fluid must consider the combined effects of diffraction, absorption, and nonlinearity [3]. The Khokhloc-Zabolotskaya-Kuznetsov (KZK) equation lays a

theoretical foundation for models to account for the combination of those all three effects [3]. Later, Zabolotskaya [5] investigate the propagation of plane and circular nonlinear Rayleigh waves in isotropic solids with an application of Hamiltonian formalism method, and an evolutionary model for the propagation of nonlinear Rayleigh waves is developed. Shull [9] investigated the harmonic generation in nonlinear Rayleigh waves [10], and later investigated nonlinear Rayleigh wave beams with diffraction considered by solving a quasi-linear equation system. Hurley [14] conducted experiments to investigate the propagation of nonlinear Rayleigh wave generated by a comb transducer and detected by an interferometer, and then Hurley demonstrate the validity of Shull's results.

Nonlinear waves have also been found promising for detecting accumulative plastic damage like fatigue damage. Among those nonlinear waves, nonlinear Rayleigh waves are an effective tool for detecting this type of damage located at near surface, since almost all propagation energy of a Rayleigh wave concentrates within a depth of two wavelengths. Many experiments have been conducted on different materials or the causes of damage. Herrmann [4] found a relationship for application of acoustic nonlinearity of longitudinal waves to Rayleigh waves, and he employed nonlinear Rayleigh waves to assess the damage due to fatigue and monotonic loading in a nickel-base superalloy. Liu [17] studied the feasibility of measuring residual stress in shot-peened aluminum plates by using nonlinear Rayleigh waves with Herrmann's theoretical relationship as a basis. Walker [11] [19] characterized fatigue damage in A36 steel also with the manner Herrmann developed.

1.3 Structure of the Thesis

Chapter 2 starts from basic equations in linear and nonlinear elasticity such as the equation of motion which leads important governing equations for wave propagation in solids, then further presents knowledge of types of waves related to Rayleigh surface waves, and finally comes to topics of nonlinearity and nonlinear Rayleigh waves. In

Chapter 3, the concepts of diffraction effect on nonlinear Rayleigh waves and the original model of diffraction in the Huygens' principle are explained. Then attentions turn to the existing models account in diffraction for nonlinear Rayleigh waves with different source conditions considered. Chapter 4 describes the required experimental setup for measuring nonlinear Rayleigh waves, the way experiments conducted, and the post-measurement analysis to obtain the normalized second harmonic amplitude at various propagation distances. Finally, a proposed method as well as comparisons of measurement results and theoretical models are presented and discussed in chapter 5. The final conclusion of this thesis is given in chapter 6, and some possible extension research topics are also proposed.

CHAPTER 2

GENERATION OF NONLINEAR RAYLEIGH WAVES

Within the frame of isotropic elasticity theory, we first derive governing equations and observe the wave phenomena in infinite space. Different types of bulk waves are first discussed and, by introducing the Snell's law and behaviors of reflection and refraction at the interface of two joined half spaces, our attention turns to the formation of Rayleigh surface wave. Afterward, the phenomenon of nonlinear Rayleigh waves followed by the associated acoustic nonlinearity is introduced to give a basic idea of the relation between nonlinear Rayleigh waves and associated acoustic nonlinearity. Contents in this chapter are based on Achenbach [1] and Graff [2].

2.1 Elasticity

2.1.1 Basic Equations

Within the restrictions of small strain, the following equations can be dirived, with symmetric stress tensor $\tau_{ij} = \tau_{ji}$ symmetric strain tensor $\varepsilon_{ij} = \varepsilon_{ji}$ and asymmetric rotation strain $\omega_{ij} = -\omega_{ji}$ for a homogenous isotropic elastic solid:

$$\tau_{ij,j} + \rho f_i = \rho \ddot{u}_i \tag{2.1}$$

$$\tau_{ij} = \lambda \varepsilon_{kk} \delta_{ij} + 2\mu \varepsilon_{ij} \tag{2.2}$$

$$\varepsilon_{ij} = \frac{1}{2}\left(u_{i,j} + u_{j,i}\right) \tag{2.3}$$

$$\omega_{ij} = \frac{1}{2}\left(u_{i,j} - u_{j,i}\right) \tag{2.4}$$

where ρ is the mass density, $\delta_{ij} = \begin{cases} 1, & i = j \\ 0, & i \neq j \end{cases}$ the Kronecker delta, and λ and μ the Lame's constants. The notation" $\ddot{}$ " is the second order differentiation of the argument

with respect to time. Substituting Eq. (2.2) and (2.3) into (2.1) gives us the equation of motion in terms of particle displacement u_i, which is also known as Navier's equation:

$$(\lambda + \mu)u_{j,ji} + \mu u_{i,jj} + \rho f_i = \ddot{u}_i \tag{2.5}$$

where f_i is the component i of body forces. Eq. (2.5) can also be represented in vector expression:

$$(\lambda + \mu)\nabla\nabla \cdot \boldsymbol{u} + \mu\nabla\text{^}2\,\boldsymbol{u} + \rho\boldsymbol{f} = \rho\ddot{\boldsymbol{u}} \tag{2.6}$$

Throughout this paper the bold characters indicate a vector, i.e. $\boldsymbol{u} = u_x\hat{\imath} + u_y\hat{\jmath} + u_z\hat{k}$. Yet an alternative form of this equation makes its physical meaning more explicitly displayed than Eq. (2.5). Let us define the notation $\Delta = \nabla \cdot \boldsymbol{u} = \varepsilon_{11} + \varepsilon_{22} + \varepsilon_{33} = \varepsilon_{kk}$ as the dilatation of a small material volume. The identity of vectors $\nabla^2\boldsymbol{u} = \nabla\nabla\mathbf{u} - \nabla \times \nabla \times \boldsymbol{u}$ and the rotation strain vector $\boldsymbol{\omega} = \frac{1}{2}\nabla \times \boldsymbol{u}$ give a way to insight the equation:

$$(\lambda + 2\mu)\nabla\Delta - 2\mu\nabla \times \boldsymbol{\omega} + \rho\boldsymbol{f} = \rho\ddot{\boldsymbol{u}} \tag{2.7}$$

The first term is associated with dilatation, while the second is associated with rotation.

2.1.2 Wave Equations

At this point, although Navier's equation in vector notation with the rotation strain vector makes its physical meaning more obvious, we still cannot easily see the wave characters from Eq. (2.7). By introducing Helmholtz decomposition

$$\boldsymbol{u} = \nabla\Phi + \nabla\mathbf{H} \tag{2.8}$$

which decouples the displacement vector with a scalar potential Φ and a vector potential **H,** an even more apparent form is obtainable, since four potential functions (Φ, H_x, H_y, H_z) are introduced to describe the three displacement components, $\nabla \cdot \mathbf{H} = 0$ is needed. This additional condition enables the three components of $\boldsymbol{u}$ to be uniquely determined by four components, which are Φ and three components of **H**. (see section 3.5 in [1] for the proof)

In a similar way, we can also express the body force with Helmholtz decomposition

$$\boldsymbol{f} = \nabla f + \nabla \boldsymbol{B}, \text{ and } \nabla \cdot \boldsymbol{B} = 0 \tag{2.9}$$

Substituting Eq. (2.8) and (2.9) and regrouping give the first step

$$\nabla\left[(\lambda + 2\mu)\nabla^2\Phi + \rho f - \rho\ddot{\Phi}\right] + \nabla \times \left(\mu\nabla^2\mathbf{H} + \rho\mathbf{B} - \rho\ddot{\mathbf{H}}\right) = 0 \tag{2.10}$$

Recalling the identity of vector, both terms in the brackets of Eq. (2.10) should vanish individually, which brings us to obtain two uncoupled equations

$$\nabla^2\Phi + \frac{1}{c_1^2} f - \frac{1}{c_1^2}\ddot{\Phi} = 0 \tag{2.11}$$

$$\nabla^2\mathbf{H} + \frac{1}{c_2^2}\mathbf{B} - \frac{1}{c_2^2}\ddot{\mathbf{H}} = 0 \tag{2.12}$$

with $c_1 = \sqrt{\frac{(\lambda+2\mu)}{\rho}}$, $c_2 = \sqrt{\frac{\mu}{\rho}}$.

At this point, with the body forces being ignored, each of the equations is what we can recognize as wave equation. More explanation will be given in the next section.

2.2 Wave Phenomenon

2.2.1 Dilatational and distortional waves

Consider Eq. (2.6) again. Taking divergence ($\nabla\cdot$) on both sides of the equation and in absence of body force, the displacement equations of motion become

$$(\lambda + \mu)\nabla \cdot (\nabla\nabla \cdot \boldsymbol{u}) + \mu\nabla \cdot (\nabla^2\boldsymbol{u}) = \rho\nabla \cdot \ddot{\boldsymbol{u}} \tag{2.13}$$

Given $\nabla\nabla=\nabla^2$, $\nabla\cdot(\nabla^2\mathbf{u})=\nabla^2(\nabla\cdot\mathbf{u})$ and $\nabla\cdot\mathbf{u}=\Delta$, we can rewrite Eq. (2.13) in terms of dilatation Δ

$$(\lambda + 2\mu)\nabla^2\Delta = \rho\ddot{\Delta} \tag{2.14}$$

or

$$\nabla^2\Delta = \frac{1}{c_1^2}\frac{\partial^2\Delta}{\partial t^2} \tag{2.15}$$

with a propagation velocity $c_1 = \sqrt{\frac{(\lambda+2\mu)}{\rho}}$. This form is more familiar since it is exactly the well-recognized scalar wave equation for the variation of dilatation, or the change in volume, propagating at velocity c_1.

On the other hand, if the operation is curl ($\nabla\times$) instead of divergence, we obtain another wave equation by the identity that curl of gradient of a scalar is zero:

$$\nabla^2\boldsymbol{\omega} = \frac{1}{c_2^2}\frac{\partial^2\boldsymbol{\omega}}{\partial t^2} \tag{2.16}$$

where the propagation velocity c_2 is given by $c_2 = \sqrt{\frac{\mu}{\rho}}$. The vector $\boldsymbol{\omega} = \frac{1}{2}\nabla\times\boldsymbol{u}$ was defined earlier as rotation vector, so we can associate Eq. (2.16) with shear perturbation.

Now let us go back to the Eq. (2.11) and (2.12). It can be seen that the scalar potential can be related to dilatational motion while the vector potential is the counterpart of rotational part. Dilatational waves, involving no rotation, propagate at c_1, while rotational waves, involving no volume changes, propagate at c_2 [2]. It has also been found that these waves travel with different velocities in a solid medium. The ratio between these two kinds of velocities can be written as

$$\kappa = \frac{c_1}{c_2} = \sqrt{\frac{\lambda+\mu}{\rho}} = \sqrt{\frac{2-2\nu}{1-2\nu}}$$

where ν is Poisson's ratio of the solid medium. Since the restriction $0\leq\nu\leq0.5$ holds, κ is always greater than 1 and thus $c_1>c_2$.

2.2.2 Harmonic waves

There are many waveforms: harmonic (sinusoidal), impulse, sawtooth, shock waves, ect. Of the most general one for simple analysis is harmonic waves. We shall first consider the case of the longitudinal wave equation in one-dimension as our example, $\nabla^2 u = \frac{1}{c_1^2}\ddot{u}$, where u is the displacement and c_1 is the longitudinal wave velocity. By

using the method of separation of variables to solve the equation, we can obtain and choose the expression for the longitudinal displacement of the form

$$u(x,t) = A\cos[k(x-ct)] \tag{2.17}$$

where the amplitude A is independent of x and t and the k the wavenumber. Eq. (2.17) is a specific form of the general form $f(x-ct)$ (the D'Alembert general solution) and this may be shown to represent a wave traveling in the positive x direction. The argument $k(x-ct)$ in the cosine is called phase of the wave. We may notice that as time increases, increasing the value of x is required to maintain the phase constant. Therefore, it appears that points of constant phase are propagated with the phase velocity c_1. At any instant t, $u(x,t)$is a periodic function of x with wavelength $\lambda = \frac{2\pi}{k}$. At any position x the displacement $u(x,t)$ is time-harmonic with time period $T = \frac{2\pi}{\omega}$, where ω is circular frequency defined as $\omega = kc$. The relations and definitions are summarized as following:

Table 2.1: Notations for wave propagation

A	amplitude
k	wavenumber
c	phase velocity
T	period
ω	circular frequency
λ	wavelength
f	frequency

$$\omega = kc, \qquad \omega = 2\pi f, \qquad T = \frac{1}{f}, \qquad \lambda = \frac{2\pi}{k}$$

For mathematical convenience we generally employ exponential expression of Eq. (2.17) instead of sinusoids:

$$u(x,t) = Ae^{i(k(x-ct))} \tag{2.18}$$

where $i = \sqrt{-1}$. Unless stated exclusively, it is supposed to consider this form and is understood that the real or imaginary part of Eq. (2.18) is to be taken for the physical interpretation of the solution.

2.2.3 Plane waves

A plane wave is a propagating disturbance where the motion of every particle in the planes perpendicular to the direction of propagation is the same. For such a disturbance, every particle in this plane maintains its phase constant. In three-dimensional cases, we may write a particle displacement function of a plane wave as follows:

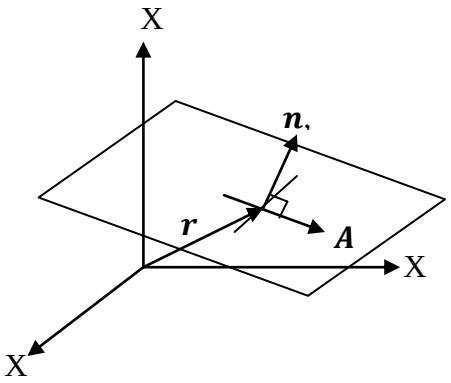

Figure 2.1: Plane wave propagating in three dimensions

$$\boldsymbol{u} = \boldsymbol{A} f(\boldsymbol{nr} - ct) \tag{2.19}$$

or in indicial notation

$$u_{i=} A_i f(n_k x_k - ct) \tag{2.20}$$

$$\varphi = n_k x_k - ct$$

, where $(\boldsymbol{nr} - ct)$ is the phase φ , $\boldsymbol{n}$ the normal of the plane, $\boldsymbol{r}$ the position vector , c the phase velocity and $\boldsymbol{A}$ the amplitude of the particle displacement in the plane of the wave. Here the function *f* can be any traveling wave function, not limited to harmonic waves. Given a disturbance of time-harmonic plain wave, the displacement function will be $\boldsymbol{u} = \boldsymbol{A} e^{ik(\boldsymbol{nr} - ct)}$, where the boldface indicates vectors.

With the previous knowledge of dilatational and distortional waves, we have learned two types of waves traveling in a solid medium. Our further investigation in the next section will be based on plane waves.

2.2.4 Wave types (P, SH and SV Waves)

Substituting plane wave Eq. (2.20) into the Navier's equation Eq. (2.5) with body forces ignored and the help of

$$u_{i,j} = A_i \frac{\partial f}{\partial x_j} = A_i \frac{\partial f}{\partial \varphi}\frac{\partial \varphi}{\partial x_j} = A_i f' n_j \tag{2.21.a}$$

$$u_{i,jj} = A_i f'' n_j n_j = A_i f'', \;\; n_j n_j = 1 \tag{2.21.b}$$

$$u_{j,ji} = A_j f'' n_j n_i, \quad \ddot{u}_i = c^2 A_i f'' \tag{2.21.c}$$

the governing equation reduces to

$$(\lambda + \mu) A_i n_j n_i + \mu A_i = \rho c^2 A_i \quad \text{(i and j =1, 2, 3)} \tag{2.22}$$

Expanding Eq. (2.22) gives us

$$\begin{bmatrix} \xi & & & & & & & & \\ & \eta & & & 0 & & & 0 & \\ & & \eta & & & & & & \\ & & & \eta & & & & & \\ & 0 & & & \xi & & & 0 & \\ & & & & & \eta & & & \\ & & & & & & \eta & & \\ & 0 & & & 0 & & & \eta & \\ & & & & & & & & \xi \end{bmatrix} \begin{bmatrix} A_1 \\ A_1 \\ A_1 \\ A_2 \\ A_2 \\ A_2 \\ A_3 \\ A_3 \\ A_3 \end{bmatrix} = 0 \tag{2.23}$$

where $\xi = (\lambda + 2\mu - \rho c^2)$, $\eta = (\mu - \rho c^2)$.

For the nontrivial solution, the determinant of Eq. (2.23) should satisfy

$(\lambda + 2\mu - \rho c^2)(\mu - \rho c^2)^2 = 0$, and thus this results two roots

$$c_1 = \sqrt{\frac{\lambda + 2\mu}{\rho}}, \quad c_2 = \sqrt{\frac{\mu}{\rho}}.$$

Now we learn plane waves are also propagating at either dilatational or distortional wave velocity in a solid medium.

The investigation may be able to be furthered when we consider in the point of view of displacements and tractions for plane waves. Let us first consider the case that u_i is parallel to n_i, which means the direction of particle displacement and the traveling direction of the plane wave are coincident, and we have

$$A_i n_i = A_j n_j = A, \quad n_i = A_i/a \tag{2.24}$$

where a is the length of the vector $\boldsymbol{A}$, i.e. $a = |\boldsymbol{A}|$. Substituting conditions Eq. (2.24) into Eq. (2.22) results

$$(\lambda + 2\mu - \rho c^2)A_i = 0 \tag{2.25}$$

Since $n_i = \mathrm{A_i}/\mathrm{a}$, Eq. (2.21.a) can be further derived and led to the condition $\nabla \times \boldsymbol{u} = 0$.

Introducing the tractions defined by $t_i = \tau_{ij} n_j$ to the stress-strain relation in Eq. (2.2) and the strain-displacement relation in Eq. (2.3), tractions can be represented in terms of displacement

$$t_i = \left[\lambda u_{k,k}\delta_{ij} + \mu\left(u_{i,j} + u_{j,i}\right)\right]n_j$$

or, together with Eq. (2.21.a) and Eq. (2.24), the above becomes

$$t_i = (\lambda + 2\mu)Af' n_i \tag{2.26}$$

Eq. (2.26) concludes that tractions are parallel to the wave normal when the displacements are in the direction of the wave normal and that such a wave will propagate as fast as at the dilatational wave velocity $\mathrm{c_1}$.

Let us turn to another case: u_i is perpendicular to n_i, and we have the condition

$$A_j n_j = 0 \tag{2.27}$$

By following the similar procedure to the previous case, we have

$$(\mu - \rho c^2) = 0 \tag{2.28}$$

and it can be shown that $\nabla \cdot \boldsymbol{u} = 0$. The tractions are simplified to be

$$t_i = \mu A_i f'$$

In this case, tractions are shown not to be parallel to the wave normal but the displacements, which are perpendicular to the wave normal traveling at the distortional wave velocity c_2.

At the end of the section, we approach the problem by simply assuming that the disturbances are simple time harmonic waves traveling in each coordinate axis,

$$u_1 = Ae^{ik(x-ct)},\ \ u_2 = Be^{ik(x-ct)},\ \ u_3 = Ce^{ik(x-ct)} \tag{2.29}$$

Substituting (2.29) back into Eq. (2.5) leads to (without body forces)

$$k^2[(\lambda + 2\mu) - \rho c^2]A = 0 \tag{2.30a}$$

$$\mathrm{k}^2(\mu - \rho \mathrm{c}^2)\mathrm{B} = 0 \tag{2.30b}$$

$$k^2(\mu - \rho c^2)C = 0 \tag{2.30c}$$

When the wave travels at the speed of c_1, only the Eq. (2.30a) is satisfied, which means the motion is purely longitudinal because of the requirement B=C=0; when the wave travels at c_2, either the Eq. (2.30b) or (2.30c) will survive and thus the motion is purely transverse. One should notice that in the second case B and C are independent of each other. Generally, the purely longitudinal wave motion is termed primary wave (P), while the purely transverse wave motion is usually called secondary wave or shear wave (S). The purely transverse motion may be specified to be shear horizontal wave (SH) or shear vertical wave (SV), depending on the direction of particle motion (or polarization) with respect to the given coordinate system [1].

2.3 Rayleigh Surface Waves

The basic ideas of wave equation have been demonstrated with various approaches in the previous section, and so far they are all considered in an infinite space. From now on, our investigation moves onto wave phenomena in a semi-infinite solid, a space with only $\mathbf{x_2} > \mathbf{0}\ \boldsymbol{or}\ \boldsymbol{y} > 0$ and with $\mathbf{x_2}$ or $\mathbf{y}$ axis increasing downward (Figure

2.2). Some phenomena which do not exist in an infinite space occur in this semi-infinite space.

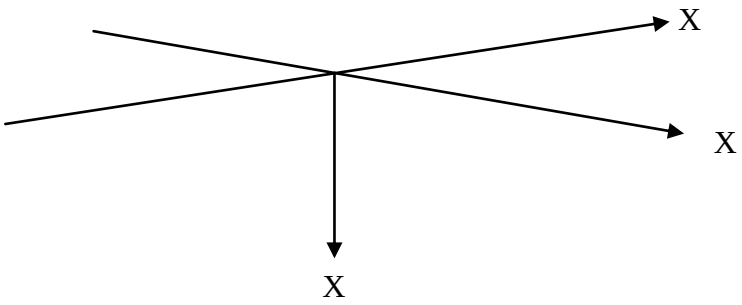

Figure 2.2: Semi-infinite space

For a quick and simple capture of knowledge of Rayleigh surface wave, we only start from essential phenomenon, and then investigate the formation of surface waves.

2.3.1 Reflection of P and SV Waves

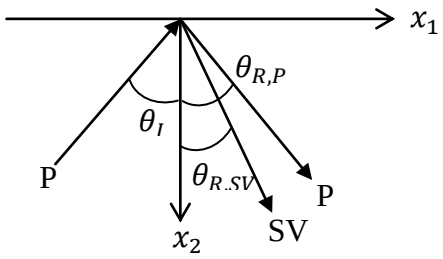

Figure 2.3: Reflection of P waves

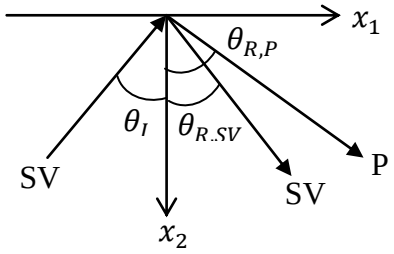

Figure 2.4: Reflection of SV waves

As we send an incident P wave obliquely to a stress-free ($\tau_{21} = \tau_{22} = 0$) surface of a semi-infinite solid medium (Figure. 3, 4), the P wave reflects not only P wave but also SV wave. Similarly, an incident SV wave triggers reflections of both P and SV wave at the surface $x_2 = 0$. The displacements of the incident harmonic plane wave can be written as

$$u = Ade^{ik(x_1 p_{1+} x_2 p_2 - ct)} \tag{2.31}$$

where $\boldsymbol{d}$ is the unit vector of displacement, A the amplitude of displacement, $p_1 = sin\theta_I, p_2 = cos\theta_I$, and $\boldsymbol{p} = p_1\hat{\imath} + p_2\hat{\jmath}$. We can now define the wave as the P wave (or longitudinal wave) for the case

$$\boldsymbol{d} = \boldsymbol{p}, \quad c = c_1$$

For a SV wave, we have

$$\boldsymbol{d} = \hat{k} \times \boldsymbol{p}, \quad c = c_2$$

while an SH wave will propagate if the unit vector of displacement and the phase velocity are as following:

$$\boldsymbol{d} = \hat{k}, \quad c = c_2$$

By substituting Eq. (2.31) into the Navier's equation, Eq. (2.5), with body forces ignored and the boundary conditions for a free surface $\tau_{21} = \tau_{22} = 0$ at $x_2 = 0$ considered, it can be found that the relationships between the angles of incidence and reflection can be summarized as the following table

Table 2.2: The relationships between incident and reflective angles

Reflection / Incidence	Longitudinal (P)	Vertically transverse (SV)
Longitudinal (P)	$\theta_{R,P} = \theta_I$	$sin\theta_{R,SV} = {c_2}/{c_1}\, sin\theta_I$
Vertically transverse (SV)	$sin\theta_I = {c_1}/{c_2}\, sin\theta_{R,SV}$	$\theta_{R,SV} = \theta_I$

This relationship can also be concluded by Snell's law,

$$\frac{c_1}{sin\theta_I} = \frac{c_1}{sin\theta_{R,P}} = \frac{c_2}{sin\theta_{R,SV}} \tag{2.32}$$

It should be noted that the reflection angle θ_R has a the limitation of $0 \leq \theta_R \leq \frac{\pi}{2}$. When a wave is sent at an incident angle such that the wave reflects at an angle $\theta_R = \frac{\pi}{2}$, that is, the reflected wave propagating along $x_2 = 0$, this incident angle is referred to as critical

angle θ_{Cr}. Since the angle of reflection is $\frac{\pi}{2}$ and due to its limitation, either sending the incident wave at or above the critical angle may cause reflection wave propagate along the surface. The critical angle can be calculated with Snell's law

$$\theta_{Cr} = sin^{-1}\left(\frac{c_I}{c_R}\right),$$

where c_I and c_R are the velocity of incident wave and that of reflection wave, respectively.

2.3.2 Rayleigh Surface Waves

When an incident wave is transmitted into a solid at an angle beyond the critical angle, there exists another type of wave called Rayleigh surface wave, named after Lord Rayleigh. This type of wave has the properties that disturbance decays rapidly as the distance from the surface increases and travels parallel to and along the surface for a quite long distance since the energy of disturbance is mostly trapped in the small thickness of approximately two times the wavelength from the surface.

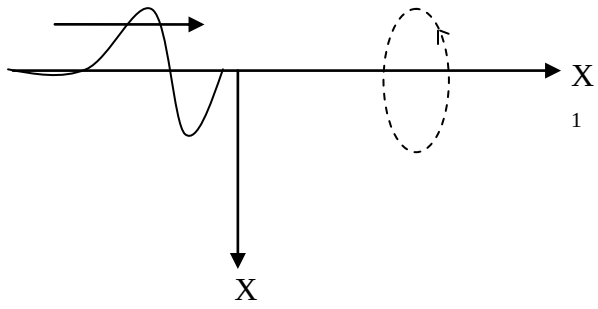

Figure 2.5: Rayleigh surface waves

To give a rather basic concept, here the two dimensional case of plane harmonic waves is considered. As shown in figure 5, suppose there is a perturbation generated and propagating at a phase velocity c along x_1 axis and exponentially decaying as the depth x_2 increases. Hence, the displacements may be postulated to be

$$u_1 = Ae^{-bx_2}e^{ik(x_1-ct)} \quad (2.33a)$$

$$u_2 = Be^{-bx_2}e^{ik(x_2-ct)} \quad (2.33b)$$

$$u_3 = 0 \tag{2.33c}$$

where b is supposed to be real and positive to keep the sense that the displacements decays with depth.

Substituting Eqs. (2.33a)-(2.33c) into the equations of motion (Combination of Eqs. (2.1), (2.2), (2.3) with body forces ignored), and this results two homogenous equations for the constant A and B. For nontrivial solutions, the determinant of this system of equations should be zero, which yields

$$[c_1^2 b^2 - (c_1^2 - c^2)k^2][c_2^2 b^2 - (c_2^2 - c^2)k^2] = 0$$

and the roots of the variable b

$$b_1 = k\left(1 - \frac{c^2}{c_1^2}\right)^{1/2},\ b_2 = k\left(1 - \frac{c^2}{c_2^2}\right)^{1/2} \tag{2.34}$$

Real positive roots are chosen, this comes with the condition $c < c_2 < c_1$. Now we have different ratios (B/A) due to the two roots of b

$$\left(\frac{B}{A}\right)_1 = -\frac{b_1}{ik}, \qquad \left(\frac{B}{A}\right)_2 = \frac{ik}{b_2}.$$

Hence, Eq. (2.33a) and (2.33b) may be rewritten in a general form

$$u_1 = [A_1 e^{-b_1 x_2} + A_2 e^{-b_2 x_2}]e^{ik(x_1 - ct)} \tag{2.35a}$$

$$u_2 = \left[-\frac{b_1}{ik} A_1 e^{-b_1 x_2} + \frac{ik}{b_2} A_2 e^{-b_2 x_2}\right] e^{ik(x_1 - ct)} \tag{2.35b}$$

Substituting Eq. (2.35a) and (2.35b) back into the expression of τ_{21} and τ_{22} in terms of displacements at $x_2 = 0$ results a pair of equation for the coefficients A_1 and A_2. Again for a nontrivial solution the determinant of coefficients $A_1$and A_2 must vanish, and thus we obtain an important equation called characteristic equation of Rayleigh wave

$$\left(2 - {c^2}/{c_2^2}\right)^2 - 4\left(1 - {c^2}/{c_1^2}\right)^{1/2} \cdot \left(1 - {c^2}/{c_2^2}\right)^{1/2} = 0 \tag{2.36}$$

where c is unknown Rayleigh wave velocity. By recalling that $\kappa = \frac{c_1}{c_2} = \sqrt{\frac{\lambda+\mu}{\rho}} = \sqrt{\frac{2-2\nu}{1-2\nu}}$, again where c_1 is the longitudinal wave phase velocity and c_2 is the transverse wave phase velocity, Eq. (2.36) may be rewritten by

$$\frac{c^2}{c_2^2}\left\{\left(\frac{c}{c_2}\right)^6 - 8\left(\frac{c}{c_2}\right)^4 + \left[24 - 16\frac{(1-2\nu)}{2(1-\nu)}\right]\left(\frac{c}{c_2}\right)^2 - 16\left[1 - \frac{(1-2\nu)}{2(1-\nu)}\right]\right\} = 0 \qquad (2.37)$$

where ν is Poisson's ratio of the solid medium. As the above equation shown, the Rayleigh wave phase velocity is independent of frequency, so Rayleigh waves are categorized as a non-dispersive wave. There are 6 roots for the Rayleigh velocity c, but only one real and positive root is in the range $0 < c < c_2$. The detail calculation of finding the root is referred to Achenbach [1] and Graff [2]. Fortunately, there is a good approximation of

$$c_R = \frac{0.862+1.14\nu}{1+\nu} c_2 \qquad (2.38)$$

where c_R is the Rayleigh wave phase velocity. In this thesis, this approximation is primarily used for simplicity of calculation. As ν varies from 0 to 0.5 (by definition of Poisson's ratio, $0 \leq \nu \leq 0.5$), the Rayleigh wave velocity monotonically increases from $0.862c_2$ to $0.955c_2$. Since the displacement components u_1 and u_2 are $\frac{\pi}{2}$ out of phase, the trajectories of the particles are ellipses (Fig. 5) and rotate counterclockwise. At the depth of about 0.2 times the wavelength the direction of rotation reverses due to u_1 changes its sign.

2.4 Nonlinear Wave Behavior in Solids

If a monochromatic wave after propagating through a material is detected only the excited frequency that it had originally, then we consider this material linear. Oppositely, when an original monochromatic wave is detected more than its original (fundamental) frequency after traveling through a material, then the material is called nonlinear material. The nonlinearity of material can be induced by inherent lattice anharmonicity and

material defects such as dislocation, precipitates, and vacancies. Previous research shows that damage due to plastic deformation including dislocations or microcracks causes the nonlinearity of material, distort initially monochromatic harmonic waves and transfer their energy to higher harmonics generated later during their traveling as well. Hence, it is possible to characterize the degree of damage in a material by relating the distortion of detected waves to the nonlinearity of material.

In this thesis, our focus is not put on the variation of nonlinearity induced by the degree of damage, so this section is only served as prerequisite knowledge for the next chapter. We first derive a parameter known as nonlinearity parameter β, which the concept is borrowed from acoustics in order to quantitatively describe the degree of nonlinearity, and then further to the case that initial disturbances are harmonic Rayleigh waves.

2.4.1 Nonlinear parameter $\boldsymbol{\beta}$

The following derivation of nonlinearity parameter in solids is primarily based on Hamilton and Blackstock [3]. Nonlinear elasticity in solids is generally described by Lagrangian (or material) coordinate. In order to connect acoustic nonlinearity to the nonlinearities in solids, it is usually more appropriate to translate formulas into material coordinate, in which the displacement $\boldsymbol{u} = \{u_1, u_2, u_3\}$ is described by the current coordinate of a particle $\boldsymbol{x}$ and its original or natural position $\boldsymbol{a}$ as a function of time t and $\boldsymbol{a}$: $\boldsymbol{u}(\boldsymbol{a}, t) = \boldsymbol{x} - \boldsymbol{a}$.

The translation of coordinate is initiated with the deformation gradient tensor within the Lagrangian description

$$L_{ij} = \frac{\partial x_i}{\partial a_j} = \delta_{ij} + \frac{\partial u_i}{\partial a_j} \tag{2.39}$$

The length of $d\boldsymbol{x}$ and $d\boldsymbol{a}$ are related by $d\boldsymbol{x}^2 - d\boldsymbol{a}^2 = d\boldsymbol{x} \cdot d\boldsymbol{x} - d\boldsymbol{a} \cdot d\boldsymbol{a} = 2d\boldsymbol{a} \cdot (E \cdot d\boldsymbol{a})$ where $E = E^T$ and thus E is symmetric, is known as Lagrangian (or Green) strain tensor defined by

$$E_{ij} = \frac{1}{2}(L^T \cdot L - I) = \frac{1}{2}\left(\frac{\partial u_i}{\partial a_j} + \frac{\partial u_j}{\partial a_i} + \frac{\partial u_k}{\partial a_i}\frac{\partial u_k}{\partial a_j}\right) \tag{2.40}$$

With Eq. (2.39) and Eq. (2.40), the introduction of nonsymmetric tensor $P = (\frac{\rho_0}{\rho})\sigma \cdot (L^{-1})^T$, known as the first Piola-Kirchhoff or Lagrangian stress tensor, and using Euler-Piola-Jacobi identity (Truesdell and Toupin, 1960, p. 246), the equations of motion can be expressed as

$$\rho_0 \frac{\partial^2 u_i}{\partial^2 t} = L_{jk} \frac{\partial P_{ik}}{\partial x_j} = \frac{\partial P_{ij}}{\partial a_j} \tag{2.41}$$

where σ is the stress tensor and ρ the density. Here the subscript "0" denotes unstressed, equilibrium state. Eq. (2.41) can be further derived in terms of E by introducing Lagrangian density $\mathcal{L} = \frac{1}{2}\rho_0 v^2 - \rho_0 W$, and we obtain

$$P = \rho_0 L \cdot \frac{\partial W}{\partial E} \tag{2.42}$$

where W is the specific strain energy of the elastic body per unit mass.

Now the relationship between strain energy and Lagrangian stress tensor needs to be established. The strain energy is assumed to have the following expansion for small strains

$$\rho_0 W = \frac{1}{2!} C_{ijkl} E_{ij} E_{kl} + \frac{1}{3!} C_{ijklmn} E_{ij} E_{kl} E_{mn} + \cdots \tag{2.43}$$

Substituting Eq. (2.43) into Eq. (2.42) results

$$P_{ij} = C_{ijkl} \frac{\partial u_k}{\partial a_l} + \frac{1}{2} M_{ijklmn} \frac{\partial u_k}{\partial a_l}\frac{\partial u_m}{\partial a_n} + \frac{1}{3} M_{ijklmnpq} \frac{\partial u_k}{\partial a_l}\frac{\partial u_m}{\partial a_n}\frac{\partial u_p}{\partial a_q} + \cdots \tag{2.44}$$

where $M_{ijklmn} = C_{ijklmn} + C_{ijln}\delta_{km} + C_{jnkl}\delta_{im} + C_{jlmn}\delta_{ik}$. The expression for the higher order coefficient $M_{ijklmnpq}$ is given by Thurston (1984).

In the absence of viscosity, the expanded stress-strain relationship Eq. (2.44) and the equations of motion Eq. (2.41) together express the expanded equations of motion in the material coordinate

$$\rho_0 \frac{\partial^2 u_i}{\partial t^2} = \frac{\partial^2 u_k}{\partial a_j \partial a_l}\left(C_{ijkl} + M_{ijklmn}\frac{\partial u_m}{\partial a_n} + M_{ijklmnpq}\frac{\partial u_m}{\partial a_n}\frac{\partial u_p}{\partial a_q} + \cdots\right) \tag{2.45}$$

For a purely longitudinal motion, consider $u_2 = u_3 = 0$ and $\boldsymbol{a} = a_1$, and this yields Eq. (2.45) to be

$$\frac{\partial^2 u_1}{\partial t^2} = c_1^2 \frac{\partial^2 u_1}{\partial a^2} h\left(\frac{\partial u_1}{\partial a}\right) \tag{2.46}$$

where $c_1 = \sqrt{\frac{(\lambda+2\mu)}{\rho_0}}$ is the linearized longitudinal phase velocity as described before and

$$h(\xi) = 1 + \left(3 + \frac{C'_{111}}{\rho_0 c_2^2}\right)\xi + \frac{1}{2!}\left(3 + \frac{3C'_{111}}{\rho_0 c_2^2} + \frac{C'_{1111}}{\rho_0 c_2^2}\right)\xi^2 + \cdots$$

in which ξ is and C' is in the Voigt's notation and its relation to original elastic coefficient C is as the following table:

Table 2.3: The relation between Voigt's notation and original elastic coefficients

$C_{ijkl} = C'_{IJ}, C_{ijklmn} = C'_{IJK} \cdots$	
C	C'
ij ⋯	I, J, K ⋯
11	1
22	2
33	3
23	4
31	5
12	6
I, J, K ⋯ ∈ {1,2,3,4,5,6}	

Eq. (2.46) can be solved by following a similar procedure shown in section 3.1 of Ch. 3 in Hamilton and Blackstock [3]. The wave speed relative to the reference configuration is $c_{ref} = c_1 h^{1/2}\left(\frac{\partial u_1}{\partial a}\right)$. According to Hamilton and Blackstock [3], the speed in the actual space then is found to be $c_1 + \beta v + \cdots$, where $\beta = -(\frac{3}{2} + \frac{C'_{111}}{2\rho_0 c_1^2})$ is the coefficient of nonlinearity and v is the particle velocity in a_1 direction.

By employing simple perturbation analysis method, given a displacement source excitation $u_1 = u_0 \sin \omega t$ and $u_2 = u_3 = 0$, we obtain

$$u(a,t) = u_0 \sin\varphi + \frac{\beta a}{8}\left(\frac{\omega u_0}{c_l}\right)^2 \cos 2\varphi + \cdots$$

$$= A_1 \sin\varphi + A_2 \cos 2\varphi + \cdots$$

where $\varphi = \omega t - k_1 a$ and $k_1 = \frac{\omega}{c_1}$ is the wavenumber of longitudinal wave. As a conclusion, nonlinearity parameter β for a solid medium may now be evaluated by

$$\beta = \frac{8c_1^2 A_2}{\omega^2 a A_1^2} \tag{2.47}$$

where a can actually be considered as propagation distance of the wave. This method provides us a more intuitive and convenient way to evaluate nonlinearity since the amplitude of the second harmonic grows in direct proportion to the propagation distance. However, one should also notice that this method is only applied to longitudinal waves in solids due to the assumptions made at the beginning. In the next section, a series of derivation will be made to enable Eq. (2.47) to be also applicable in the case of Rayleigh waves.

2.4.2 Nonlinear Rayleigh Waves

In this section the derivation is based on Herrmann et al. [4], Zabolotskaya[5] and Viktorov [6]. Consider a sinusoidal Rayleigh wave is excited and propagating along the x axis in a half-space (semi-infinite space) and the z axis is pointing downward into the material. Since the wave is considered to be plane, there is no variation along y direction, which means $\frac{\partial}{\partial y} = 0$. According to Viktorov [6] and Herrmann et al. [4], we may first assume the particle displacement in terms of scalar potential φ and vector potential ψ

$$u = \nabla \cdot \varphi + \nabla \times \psi \tag{2.48a}$$

$$u_x = \frac{\partial \varphi}{\partial x} - \frac{\partial \psi_y}{\partial z} \tag{2.48b}$$

$$u_z = \frac{\partial \varphi}{\partial z} + \frac{\partial \psi_y}{\partial x} \tag{2.48c}$$

We postulate that the solutions for φ and $\boldsymbol{\psi}$ satisfying equation of motion and corresponding to a plane harmonic wave propagating in the positive x direction:

$$\varphi = -i\frac{A_1}{k_R}e^{-pz}e^{i(k_R x-\omega t)} \tag{2.49a}$$

$$\psi = -i\frac{B_1}{k_R}e^{-sz}e^{i(k_R x-\omega t)} \tag{2.49b}$$

where $p^2 = k_R^2 - k_l^2$; $s^2 = k_R^2 - k_t^2$; and k_R, k_l and k_t are the wavenumbers of Rayleigh, longitudinal and transverse waves, respectively. With the result of Eq. (2.49a) and (2.49b), substituting Eq. (2.48a) to equation of motion and then applying the stress-free surface boundary conditions results the relationship

$$A_1 = -i\frac{2k_R p}{k_R^2 + s^2}B_1 \, .$$

Since Rayleigh waves are the superposition of longitudinal and shear waves that propagate with the same trace velocity along a stress free surface, the displacement components may be decomposed into their longitudinal and shear contributions. Once the scalar and vector potentials and the relationship between their coefficients are derived, the displacement in x and z directions can be obtained by employing Eq. (2.48b) and (2.48c)

$$u_{x1} = A_1\left(e^{-pz} - \frac{2ps}{k_R^2+s^2}e^{-pz}\right)e^{i(k_R x-\omega t)} \tag{2.50a}$$

$$u_{z1} = iA_1\frac{p}{k_R}\left(e^{-pz} - \frac{2ps}{k_R^2+s^2}e^{-sz}\right)e^{i(k_R x-\omega t)} \tag{2.50b}$$

where the numbers in the subscript of displacement denotes the order of harmonic. In a medium having weak quadratic nonlinearity, displacements of the second harmonic Rayleigh waves at a sufficiently large distance (or far field) can be described as: [4]

$$u_{x2} \approx A_2\left(e^{-2pz} - \frac{2ps}{k_R^2+s^2}e^{-2sz}\right)e^{i2(k_R x-\omega t)} \tag{2.51a}$$

$$u_{z2} \approx iA_2\frac{p}{k_R}\left(e^{-2pz} - \frac{2k_R^2}{k_R^2+s^2}e^{-2sz}\right)e^{i2(k_R x-\omega t)} \tag{2.51b}$$

"The acoustic nonlinearity for the shear wave in an isotropic material vanishes due to the symmetry of the third order elastic constants, so the longitudinal wave component is solely responsible for the acoustic nonlinearity (or the higher harmonics) in Rayleigh waves [4]." Therefore, for Rayleigh waves near the surface, the in-plane amplitudes of displacement (u_x) for fundamental and second harmonic can be related to the nonlinearity parameter for longitudinal wave in a similar manner of Eq. (2.47)

$$A_2 = \frac{\beta\omega^2 x}{8c_1^2} A_1^2 \tag{2.52}$$

where x is propagation distance and c_1 is longitudinal wave velocity. In the experiments of this thesis, out-of plane particle velocity (or equivalent displacement) at the surface are measured and analyzed for the frequency spectrum through fast Fourier transform (FFT). By Eq. (2.51a), (2.51b) and (2.52), the relationship between nonlinearity parameter the amplitudes of fundamental and second harmonic can be expressed as

$$\frac{u_{z2}|_{z=0}}{u_{z1}^2|_{z=0}} = \frac{\beta k_1^2 x}{8i(p/k_R)[1-2k_R^2/(k_R^2+s^2)]} \tag{2.53}$$

, or

$$\beta = \frac{8i}{k_1^2}\frac{1}{x} \cdot \frac{u_{z2}|_{z=0}}{u_{z1}^2|_{z=0}} \cdot \frac{p}{k_R}\left(1 - \frac{2k_R^2}{k_R^2+s^2}\right) \tag{2.54}$$

The second term in the bracket of the above equation reveals the contribution of shear wave component interacting with the longitudinal wave component, but the shear wave alone does not cause nonlinearity.

CHAPTER 3

DIFFRACTION EFFECT ON NONLINEAR RAYLEIGH WAVES

3.1 Diffraction Effect

3.1.1 Basic Concept of Diffraction

Diffraction is a prevalent effect which can be found in the any kinds of wave motions including light, electromagnetic waves and sound, and can be seen as one of characteristics of wave motions. The cause of formulation is basically associated with the addition of waves emitted from a series of point sources. As a result this addition of all waves along all unobstructed paths bends or distorts the original wavefront. Such a physical phenomenon usually occurs when waves encounter a small obstacle or a small opening, where the "small" is relatively compared to the wavelength of incidence waves.

The well-known Huygens' principle [8] for the wave theory of light provides a good basis model for predicting the diffraction effect. French physicist Augustin-Jean Fresnel combined Huygens' principle with his own principle of interference, and proposed a modified formula. Later, Kirchhoff gave a rigorous mathematical foundation for Huygens' principle.

The basic concept of diffraction proposed by Huygens can be described as that a wavefront could be modeled as a series of wavelets. These wavelets superimpose and interfere with each other as well as boundaries to form more complicated wavefronts.

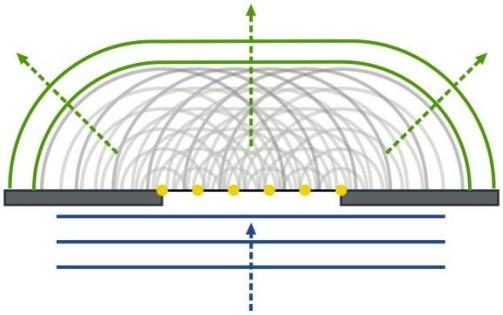

Figure 3.1: Wave diffraction in the manner of Huygens and Fresnel [18]

Figure 3.1 demonstrates this phenomenon. Given a monochromatic incidence plane wave propagating towards an opening, usually called a slip or a gap, the opening can be regarded as a set of secondary sources of spherical waves. As waves are generated from each of point sources, these waves interact with the adjacent ones and cause a phenomenon that appeared to be a set of beams traveling in different directions due to the construction and destruction created by the superposition, or interference, of the peaks and valleys of those waves.

The size of the opening matters the degree of diffraction. When the size of the opening is small compared to the wavelength of the incidence wave, the diffraction effect is prominent, and comes to its maximum when the size of the opening close to one wavelength of the incidence wave. As the size of the opening increases, the effect becomes weaker. One can figure this with the help of figure 6 depicting that the wavefront generated by the combination of those spherical waves is observed flattened, that is, not being bended or distorted from its original shape, and more and more approaches plane waves again as they propagate further.

3.1.2 Diffraction Effects in Nonlinear Rayleigh Wave Beams

The following sections are a summary based on the results of the works by Shull et al. [9] [10] and Zabolotskaya [5]. As the Chapter 2 discussed, the phase velocity of Rayleigh surface waves is independent of frequency, which means that harmonics arise because of nonlinearity, rather than source itself, and meanwhile energy transferring from fundamental to higher harmonics. Furthermore, since the harmonics will propagate with equal velocities they interact effectively and result the nonlinear distortion of surface waves [11] [19]. This makes the prediction of beam diffraction of nonlinear Rayleigh waves more difficult. In Zabolotskaya [5], a revolutionary mathematical method for nonlinear Rayleigh waves in isotropic solids was developed to improve previous works by an application of Hamiltonian formalism. Later, Shull [9] derived analytical solutions with consideration of diffraction for nonlinear Rayleigh wave beams excited by a Gaussian line sources and numerical solutions for that generated by a uniform line source.

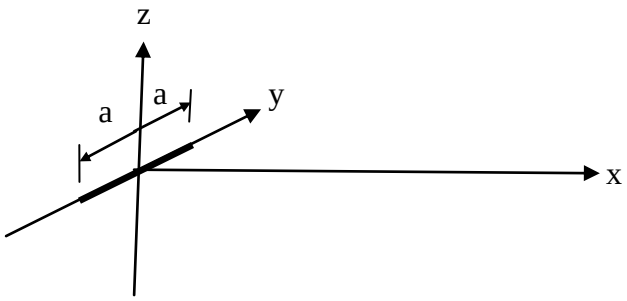

Figure 3.2: Wave propagation in a half space

When $k_0 a \gg 1$, where a is the half length of the line source, (i.e. the size of the transducer is much greater than the wavelength excited frequency) the dominant effects of diffraction is taken into account by a modification of the theory for nonlinear plane waves propagating in single direction using the parabolic approximation.

Consider a Rayleigh wave beam propagating in an isotropic solid half space ($z \leq 0$) in the + x direction [9], which is depicted as Figure 3.2. Diffraction causes the

wave beam diverge in the x-y plane; however, within the parabolic approximation, the y component of the particle motion in a directive beam is smaller order than the x component. Therefore, the Rayleigh wave beam may be considered in terms of only x- and z-direction components of particle velocity for all harmonics in this half space[9]:

$$v_x(x,y,z,t) = \frac{1}{2}\sum_{-\infty}^{\infty} v_n(x,y)u_{x,n}(z)e^{in(k_0x-\omega_0t)} \tag{3.1}$$

$$v_z(x,y,z,t) = \frac{1}{2}\sum_{-\infty}^{\infty} v_n(x,y)u_{z,n}(z)e^{in(k_0x-\omega_0t)} \tag{3.2}$$

where n denotes the order of harmonic, v_n expresses the spatial part of complex particle velocity in x-y plane, ω_0 is the excited frequency (fundamental frequency), $k_0 = \omega_0/c_R$ is the wavenumber of excited waves, and c_R is the small-signal Rayleigh wave speed. $u_{x,n}$ and $u_{z,n}$ are functions describing the variation along the depth z for the x and z components of particle velocity:

$$u_{x,n} = i(sgn\ n)[\xi_t\ exp(|n|\xi_t k_0 z) + \eta exp(|n|\xi_l k_0 z)] \tag{3.3}$$

$$u_{z,n} = exp(|n|\xi_t k_0 z) + \xi_l \eta exp(|n|\xi_l k_0 z) \tag{3.4}$$

where $\xi_t = (1-\xi^2)^{1/2}$, $\xi_l = (1-\xi^2\, c_t^2/c_l^2)^{1/2}$, $\eta = -2(1-\xi^2)^{1/2}/(2-\xi^2)$, $\xi = c_R/c_t$, c_t and c_l are the speed of transverse (shear) waves and the speed of longitudinal waves, respectively.

When diffraction is taken into account within parabolic approximation, the spectral equation describing the propagation of nonlinear Rayleigh wave beams can be written as [9]:

$$\frac{\partial v_n}{\partial x} + \frac{1}{2ink_0}\frac{\partial^2 v_n}{\partial y^2} + \alpha_n v_n$$

$$= \frac{n^2}{v_0\bar{x}}\left(2\sum_{m=n+1}^{\infty} R_{m,n-m}v_m v_{m-n}^* - \sum_{m=1}^{n-1} R_{m,n-m}v_m v_{n-m}\right) \tag{3.5}$$

where $v_n^* = v_{-n}$, (v_x and v_z are assumed to be real quantities), α_n is the attenuation coefficient at frequency $n\omega_0$, $\bar{x} = 2\zeta\rho c_R^3/\mu k_0 v_0$ is a characteristic length scale related to the shock formation distance for weakly attenuated plane waves, ρ is the density of the

material, μ is the shear modulus, v_0 is the velocity amplitude at the source, $\zeta = \xi_t + \xi_l^{-1} + \eta^2(\xi_l + \xi_l^{-1}) + 4\eta$, and the symmetric matrix R is defined as: [5]

$$R_{ml} = \frac{\alpha'}{|n|\xi_l + |l|\xi_t + |m|\xi_t} + \frac{\alpha'}{|n|\xi_t + |l|\xi_t + |m|\xi_l} + \frac{\alpha'}{|n|\xi_t + |l|\xi_l + |m|\xi_t} + \frac{\beta'}{|n|\xi_t + |l|\xi_l + |m|\xi_l} + \frac{\beta'}{|n|\xi_l + |l|\xi_t + |m|\xi_l} + \frac{\beta'}{|n|\xi_l + |l|\xi_l + |m|\xi_t} + \frac{3\gamma'}{|n|\xi_l + |l|\xi_l + |m|\xi_l}$$

where $n = l + m$, and the coefficients α', β', and γ' which depend on material properties, are as following: [5]

$$\alpha' = \alpha + \delta, \qquad \beta' = \beta,$$

$$\gamma' = \gamma + \frac{1}{3}\left[\nu + \frac{2\xi_l(\epsilon - 2\delta)}{\xi_l + \xi_t}\right],$$

$$\alpha = \eta\left(\frac{7\mu}{3} + A + 2B + K\right)(1 - \zeta_l^2)\xi_t^2/\mu,$$

$$\beta = \eta^2\left(\frac{7\mu}{3} + A + 2B + K\right)(1 - \xi_l^4)\xi_1/\mu,$$

$$\gamma = \eta^3\left[\left(\mu + \frac{A}{3}\right)(1 + \xi_l^2 + \xi_l^4) + \left(B + \frac{K}{2} - \frac{\mu}{3}\right)(1 + \xi_l^4) + \frac{C(1 - \xi_l^2)^2}{3}\right] \times (1 - \xi_l^2)/\mu$$

$$\delta = \eta\left[\left(\mu + \frac{A}{4}\right)(1 + \xi_t^2 + \xi_t^4) + \frac{A\xi_t^2}{4} + \frac{B(1 + \xi_t^4)^2}{2} + \left(\frac{K}{2} - \frac{\mu}{3}\right)(1 + \xi_t^4)\right] \times (1 - \xi_t^2)/\mu$$

$$\epsilon = \eta^2\left(\frac{7\mu}{3} + A + 2B + K\right)(1 + \xi_t^2)(1 - \xi_l^2)\xi_2/\mu$$

$$\nu = \eta^3\left(\frac{7\mu}{3} + A + 2B + K\right)(1 - \xi_l^2)\xi_l^2/\mu$$

Here K is the modulus of hydrostatic compression, λ and μ are Lame constants, and A, B, C are the third order elastic constants, and they are calculated in the following way:

$$\lambda = K - \tfrac{2}{3}\mu, \quad A = n', \quad B = m' - n'/2, \quad C = \tfrac{1}{2}(n' + 2l' - 2m')$$

where l', n', and m' refer to as l, m, n of Murnaghan constants, respectively.

The complex particle velocity for plane waves varying in x-y plane can be assumed to be an exponential function:

$$v_n(x,y) = |v_n(x,y)|e^{-i\phi_n(x,y)} \tag{3.6}$$

$$\phi_n = -tan^{-1}\left[\frac{(Im\ v_n)}{(Re\ v_n)}\right]$$

Substituting Eq. (3.6) into (3.5) yields the expression of waveforms for x and z components of particle velocity (the real part) at surface (z=0):

$$v_x(x,y,0,t) = (\xi_t + \eta)\sum_{n=1}^{\infty}|v_n(x,y)|sin[n\omega_0(t - x/c_R) + \phi_n(x,y)] \tag{3.7}$$

$$v_z(x,y,0,t) = (1 + \xi_l\eta)\sum_{n=1}^{\infty}|v_n(x,y)|cos[n\omega_0(t - x/c_R) + \phi_n(x,y)] \tag{3.8}$$

If the source is limited to a single frequency, the boundary condition at the source ($x = 0$) is

$$v_1(0,y) = w(y) \tag{3.9}$$

$$v_n(0,y) = 0,\ for\ n > 1 \tag{3.10}$$

where $w(y)$ is a complex source function.

3.2 Coupled Quasilinear Partial Differential Equations

By using Eq. (3.5), two-dimensional partial differential equations of particle velocity for the fundamental and second harmonic component (n=1 and 2) can be individually obtained and form a quasilinear system:

$$\left(\frac{\partial}{\partial x} + \frac{1}{2ik_0}\frac{\partial^2}{\partial y^2} + \alpha_1\right)v_1 = 0 \tag{3.11}$$

$$\left(\frac{\partial}{\partial x} + \frac{1}{4ik_0}\frac{\partial^2}{\partial y^2} + \alpha_2\right)v_2 = -\frac{\beta_{11}k_0}{2c_R}v_1^2 \tag{3.12}$$

where $\beta_{11} = \frac{4\mu R_{11}}{\zeta\rho c_R^2}$, $R_{11} = \frac{\alpha\prime(5\xi_l+7\xi_t)}{2(\xi_l+\xi_t)(\xi_l+3\xi_t)} + \frac{(7\xi_l+5\xi_t)}{2(\xi_l+\xi_t)(3\xi_l+\xi_t)} + \frac{3\gamma\prime}{4\xi_l}$.

Here Eq. (3.11) and (3.12) are equivalent to the equations for two-dimensional sound waves in fluids if the dimensionless coefficient $\beta_{11}$is introduced to be the coefficient of nonlinearity [9]. With consideration of the source conditions in Eq. (3.9) and (3.10), the

integral solution of quasilinear equations, Eq. (3.11) and (3.12), for fundamental and second harmonics in terms of Green's function $G(x, y|x', y')$ is represented as (the x'- y' plane is the source domain):

$$v_1(x,y) = \int_{-\infty}^{\infty} w(y') G_1(x, y|0, y')\, dy' \tag{3.13}$$

$$v_2(x,y) = -\frac{\beta_{11} k_0}{2c_R} \int_0^x \int_{-\infty}^{\infty} v_1^2(x', y') \times G_2(x, y|x', y') dy'\, dx' \tag{3.14}$$

where $G_n(x, y|x', y') = \sqrt{\frac{nk_0}{i2\pi(x-x')}} \exp(-\alpha_n(x-x') + \frac{ink_0(y-y')^2}{2(x-x')})$, and $\sqrt{i} = e^{i\pi/4}$

Next we are to discuss different analytical or numerical solutions resulted from various types of source conditions.

3.2.1 Model for Gaussian Line Source

When the source amplitude is assumed to distribute on $x = 0$ as a Gaussian function with the central peak amplitude v_0 at $y = 0$ and with limited length (radius) a, as pictured in Fig. 3.2, we can consider the source function to be:

$$v_1(0, y) = w(y),$$
$$v_n(0, y) = 0, \qquad for\ n > 1$$
$$w(y) = v_0 e^{-(y/a)^2}$$

Substituting these conditions into Eq. (3.13) and (3.14) results the analytical spatial expression of the particle velocity for fundamental and second harmonics:

$$v_1(x,y) = \frac{v_0 e^{-\alpha_1 x}}{\sqrt{1+ix/x_0}} exp\left(-\frac{\left(\frac{y}{a}\right)^2}{1+\frac{ix}{x_0}}\right) \tag{3.15}$$

$$v_2(x,y) = \frac{i\sqrt{\pi}\beta_{11} v_0^2 k_0^2 a^2}{4c_R\sqrt{i(\alpha_2 - 2\alpha_1)(x_0 + ix)}}$$
$$\times exp\left(-\alpha_2 x - \frac{2\left(\frac{y}{a}\right)^2}{1+\frac{ix}{x_0}} + i(\alpha_2 - 2\alpha_1)x_0\right)$$
$$\times \{erf\left[\sqrt{i(\alpha_2 - 2\alpha_1)(x_0 + ix)}\right]] - erf\,[\sqrt{i(\alpha_2 - 2\alpha_1)x_0}]\} \tag{3.16}$$

where $x_0 = k_0 a^2/2$ is Rayleigh distance, which is usually associated with the beginning of the farfield. We can obtain the central axis amplitude, as shown in the figure 3.3, by setting $y = 0$ in the above two equations. Our focus is put on the variation in the nearfield, and it is more convenient to observe the trend in the nearfield through normalizing the propagation distance by Rayleigh distance x_0 and the amplitudes of particle velocities by the excited amplitude v_0.

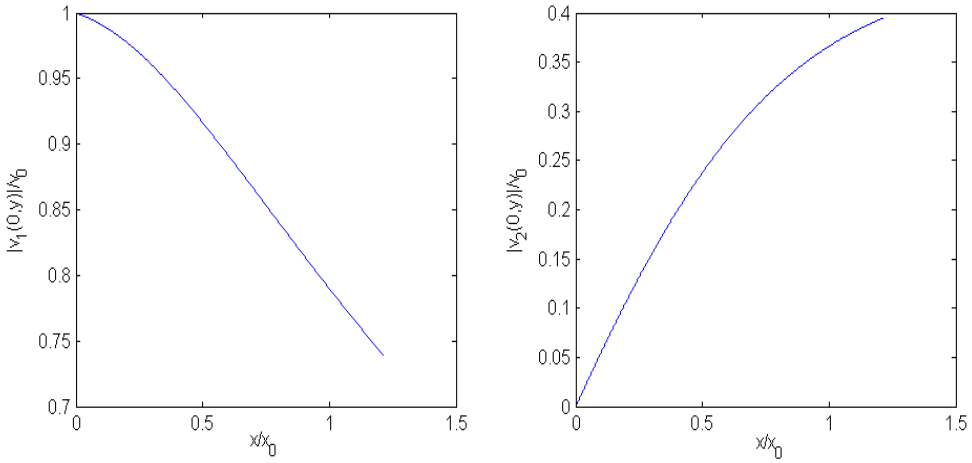

Figure 3.3: On-axis amplitudes of particle velocity for fundamental (left) and second (right) harmonics generated from a Gaussian line source

The trend of the amplitude depends on the coefficients of attenuation for fundamental and second harmonics and the constants pertaining to properties of materials. The higher coefficients of attenuation are, the faster the amplitudes decline, as expected. For the second harmonics, the larger coefficient of nonlinearity gives the front part of the curve rises faster.

3.2.2 Model for Uniform Line Source

The Now consider the case of uniform line sources, and the source condition can be written as

$$w(y) = v_0, \qquad |y| \le a$$
$$= 0, \qquad |y| > a$$

In a similar manner, by substituting these source conditions into Eq. (3.13) and (3.14), we can obtain the analytical solution for the fundamental harmonic component:

$$v_1(x,y) = \frac{v_0}{2} e^{-\alpha_1 x} \left\{ erf\left[\sqrt{\frac{ix}{x_0}}(1+\frac{y}{a})\right] + erf\left[\sqrt{\frac{ix}{x_0}}(1-\frac{y}{a})\right]\right\} \tag{3.17}$$

Figure 3.4 illustrates an example of the analytic solution of the on-axis ($y = 0$) amplitude of the fundamental waves. Here the x axis is normalized by Rayleigh distance $x_0 = k_0 a^2/2$ and the on-axis amplitude is normalized by the source amplitude in order to clearly show the tendency.

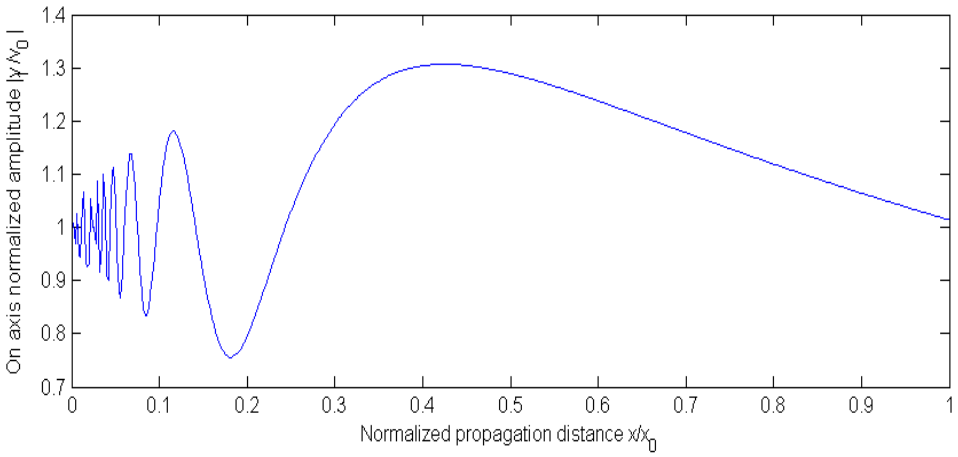

Figure 3.4: Analytic solution for the normalized on-axis particle velocity amplitude of the fundamental waves generated by a single uniform line source

However, there is no analytic solution for the second harmonic. Next, the numerical solutions are represented, and it is calculated in a pair of the system equations Eq. (3.11) and (3.12).

3.2.2.1 Original Equation

The tool in MATLAB for solving partial differential equations is used for numerically solving all following equations. To begin with, Eq. (3.11) and (3.12) are implemented with boundary conditions:

$$v_n = 0 \;\; at\; y = -1\; and\; 1\; meter,$$

$$v_1(0, y) = v_0 \quad y \leq a,$$

$$= 0 \quad y > a,$$

$$v_n(0, y) = 0 \;\; n > 1$$

Likewise, the on-axis amplitudes on $y = 0$ are investigated. In the numerical calculation, the step size of computation matters. In this case, the influence of the step size on y direction to the results dominates over that by x direction. As shown in figure 3.5, decreasing the step size (higher resolution) on y direction provides more details in the nearfield for the fundamental wave. The amplitudes of the second harmonic are observed to hardly change with different resolutions on x direction.

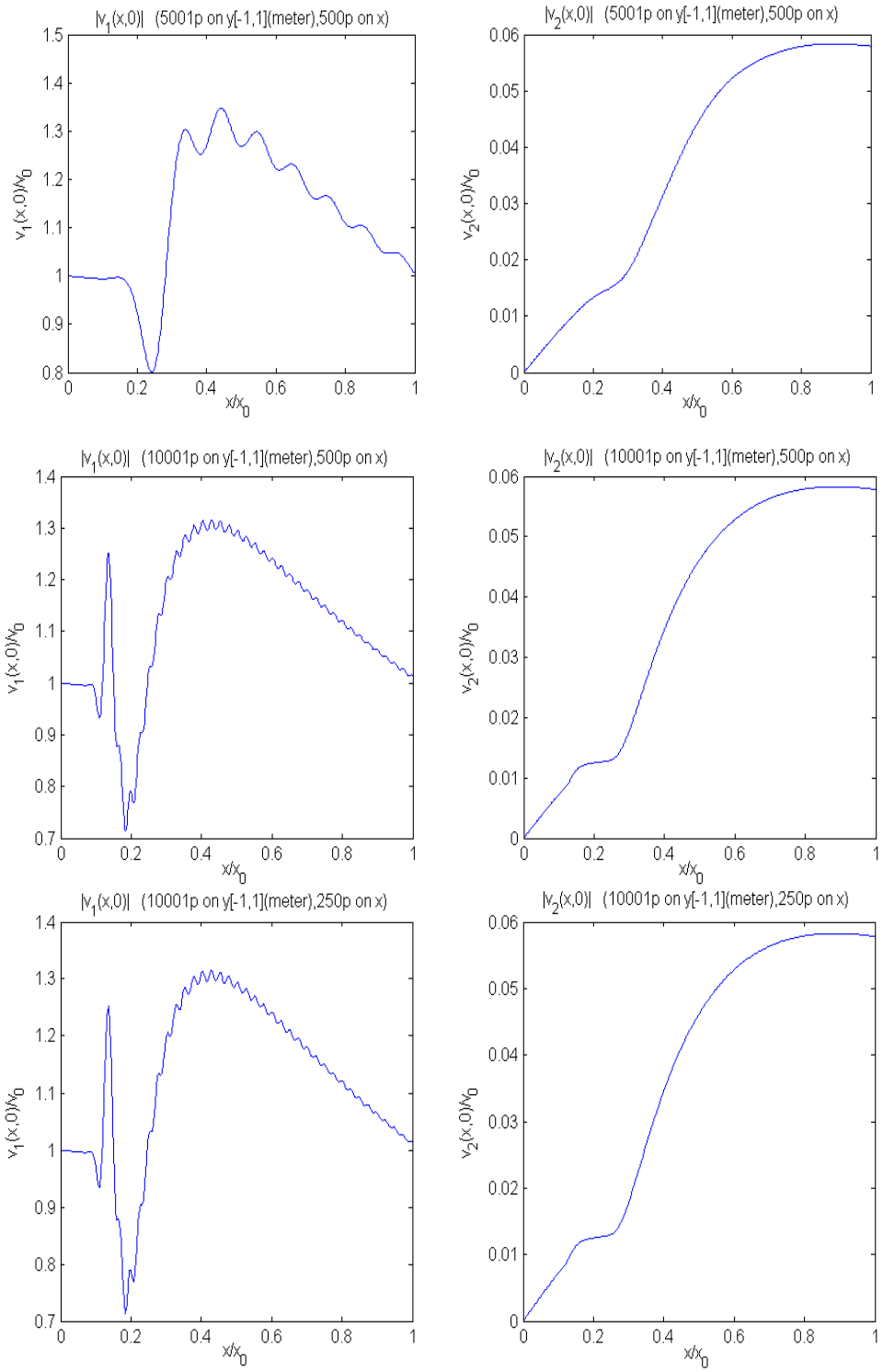

Figure 3.5: Numerical solution for the normalized on-axis particle velocity amplitudes of the fundamental harmonic, generated from a single uniform line source, and the second harmonic

3.2.2.2 Modified Equations with Normalized Variables

Although the original system equations has already provided a mathematical result which describes major phenomenon in the nearfield, the computation time dramatically increases as the resolution on y direction rises but with still insufficient detail information in the nearfield provided. By normalizing variables, the computation becomes more efficient. The result reveals more details and more approaches to the analytic solution yet with a demand of much lower resolution on y direction.

We now modify Eq. (3.5) by normalizing the following variables:

$$V_n = \frac{v_n}{v_0},\ \ X = \frac{x}{x_0},\ \ Y = \frac{y}{a},\ \ A_n = \alpha_n x_0,\ \ B = x_0/\bar{x}$$

Applying these variables to the spectral equation, Eq. (3.5), yields:

$$\frac{\partial V_n}{\partial X} + \frac{1}{4in}\frac{\partial^2 V_n}{\partial Y^2} + A_n V_n = Bn^2\left(2\sum_{m=n+1}^{N} R_{m,n-m} V_m V_{m-n}^* - \sum_{m=1}^{n-1} R_{m,n-m} V_m V_{n-m}\right) \quad (3.18)$$

The source conditions are modified to be:

$$V_1(0,Y) = 1,\ \ |Y| \le 1$$
$$= 0,\ \ |Y| > 0$$
$$V_n(0,Y) = 0,\quad n > 1$$

The numerical solution of fundamental harmonic is compared with the analytic solution. Figure 3.6 shows how factors such as resolution on Y direction, resolution on X direction, and boundary location, affect the solution outcomes of the fundamental harmonic; however, there is still no apparent change on the second harmonic as the values of these factors vary. Note that smooth resulting curves are obtained by remaining the resolution on Y direction at 0.2 and that on X direction at 400 points over a Rayleigh distance. The smooth portion shrinks as the boundaries on Y direction for computation approach the source, vice versa. Figure 3.6 also shows the analytic solution (dashed line) and three results with different boundaries for computation where the boundary condition is $V_n = 0\ for\ all\ n$. The smooth portion of the result computed with the boundaries for Y direction at $Y = -6, 6$ is larger than those computed with the boundaries at $Y = -5, 5$ or

at $Y = -4, 4$. Furthermore, there is a tendency that the trend of the curve converges to the analytic solution as the result is computed with boundaries for Y direction further from the source.

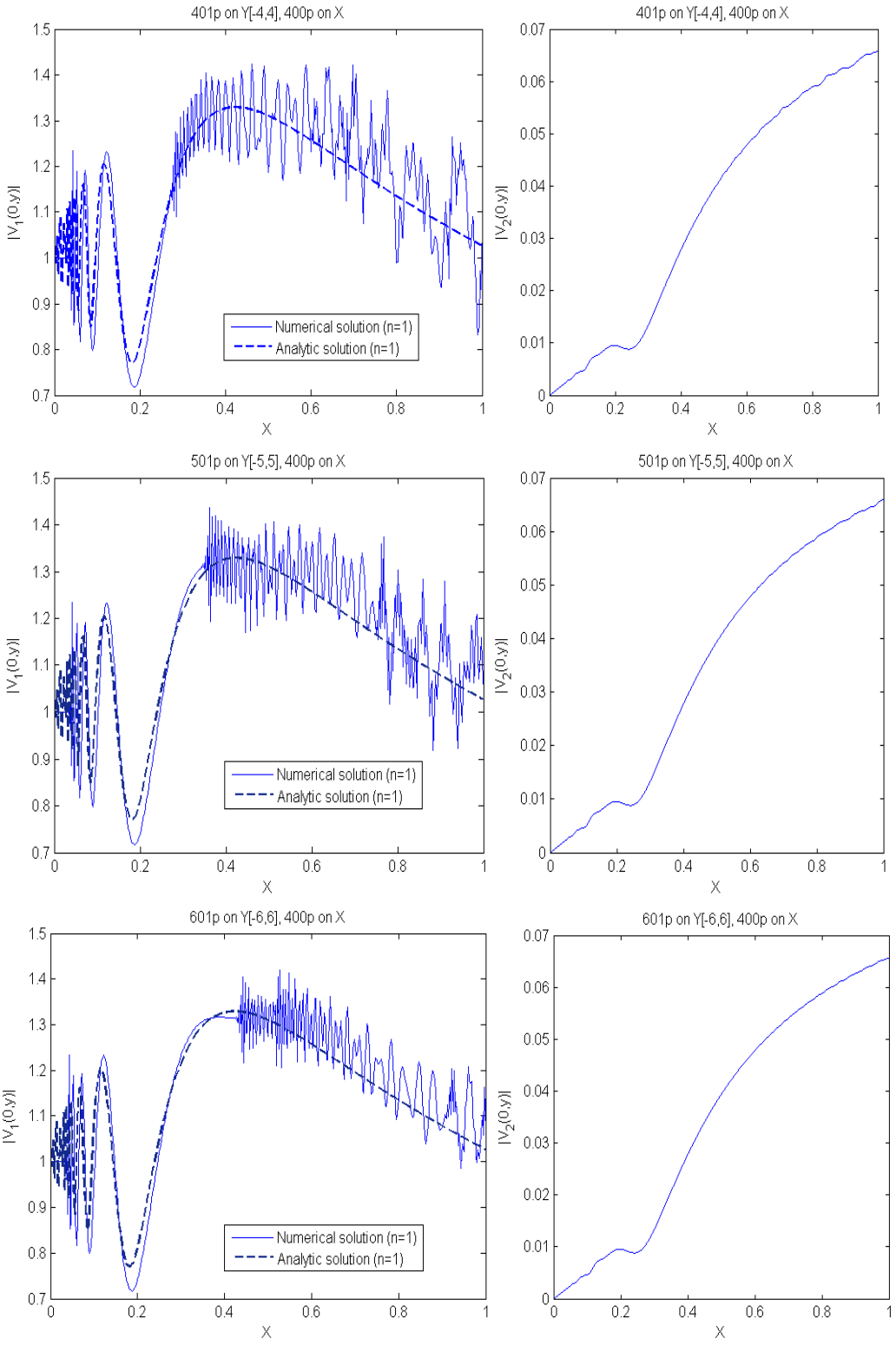

Figure 3.6: Normalized on-axis amplitudes of V_1 and V_2 computed with boundaries at different distances from the source on Y direction

3.2.2.3 Modified Equations with Normalized Variables for the Cylindrically Spreading Beams

Previous numerical solutions all shows trembling in different extents. We now introduce an even improved calculation method in which the original rectangular coordinate is mapped onto another coordinate for cylindrically spreading beams by a modification with adding a divergence parameter δ. For $\delta > 0$, the grids of new coordinate diverges from the beam axis when it is mapped back onto the original rectangular coordinate. This transformation of the reference coordinate makes the computation at the area close to farfield more efficiently than previous models do [9], and with this transformation the trembling of the curves resulted from previous equations is also mitigated.

To build the new coordinate, the normalized variables are again modified as following:

$$\bar{V}_n(X,\bar{Y}) = \sqrt{X+\delta}\,\bar{V}_n(X,Y)\,exp\left[-\frac{inY^2}{X+\delta}\right] \tag{3.19}$$

$$\bar{Y} = Y/(X+\delta) \tag{3.20}$$

Eq. (3.20) serves as a transformation by which the grid in new coordinate diverges as it corresponds to rectangular coordinate. The larger value of the δ is, the more diverged the grid of new coordinate is in the original coordinate. By following a similar manner, substituting Eq. (3.19) and (3.20) into Eq. (3.5) yields the spectral equation with respect to the new coordinate for cylindrically spreading beams:

$$\frac{\partial\bar{V}_n}{\partial X} + \frac{1}{4in(X+\delta)^2}\frac{\partial^2\bar{V}_n}{\partial\bar{Y}^2} + A_n\bar{V}_n = \frac{Bn^2}{\sqrt{X+\delta}} \times \left(2\sum_{m=n+1}^{N} R_{m,n-m}\bar{V}_m\bar{V}^*_{m-n} - \sum_{m=1}^{n-1} R_{m,n-m}\bar{V}_m\bar{V}_{n-m}\right) \tag{3.21}$$

Again, the source conditions are modified to be:

$$\bar{V}_1(0,\bar{Y}) = \sqrt{\delta}e^{i\delta\bar{Y}^2},\ \ |\delta\bar{Y}| \le 1$$
$$= 0,\ \ |\delta\bar{Y}| > 0$$

$$\bar{V}_n(0,\bar{Y}) = 0, \quad n > 1$$

With the choice of $\delta = 2.5$, the computation boundaries on $\bar{Y}$ direction are -4 and 4, and the number of differential points on $\bar{Y}$ is 1000 and 500 on $\bar{X}$, the following result is obtained and shown in $X - Y$ domain:

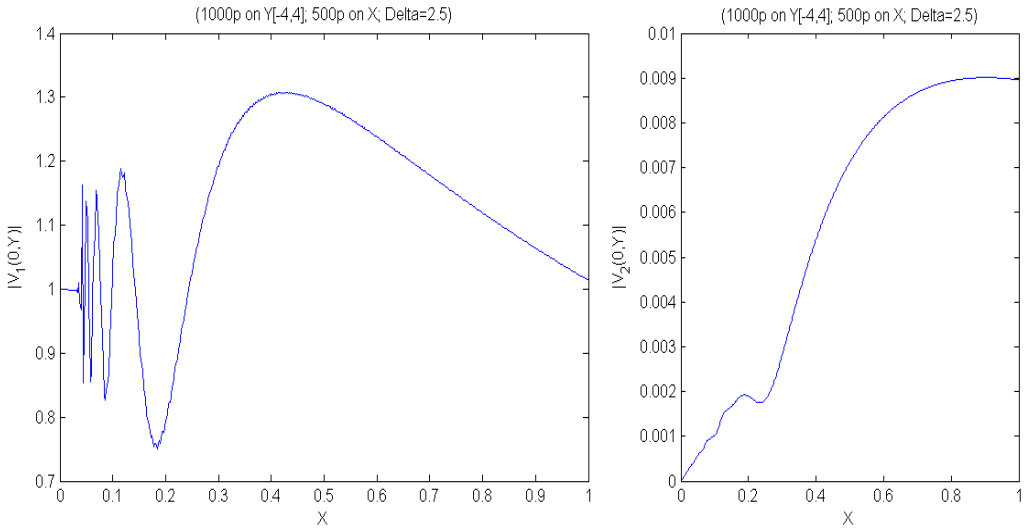

Figure 3.7: On-axis amplitudes of V_1 and V_2 computed by the equation within the cylindrically spreading coordinate

Obviously, the result of particle velocity for fundamental harmonic is more approach to the analytic solution than previous methods, and the trembling close to the Rayleigh distance on the curve is also effectively reduced. Furthermore, one can more easily see from figure 3.7 that the amplitude increases and fluctuates vigorously in front of the source until the distance as far as 0.4 times Rayleigh distance; however, the curve of second harmonic still does not show distinguishable differences from the results computed from previous equations.

In figure 3.8, the numerical solution and the analytic solution (dashed line) for the on-axis amplitude of the fundamental harmonic are compared, and one can also see the fact that this numerical solution computed with the equations within cylindrically spreading coordinate has already shown a good match with the analytic solution at the

region above approximately 0.05 times Rayleigh distance (here the Rayleigh distance is about 9.89 mm).

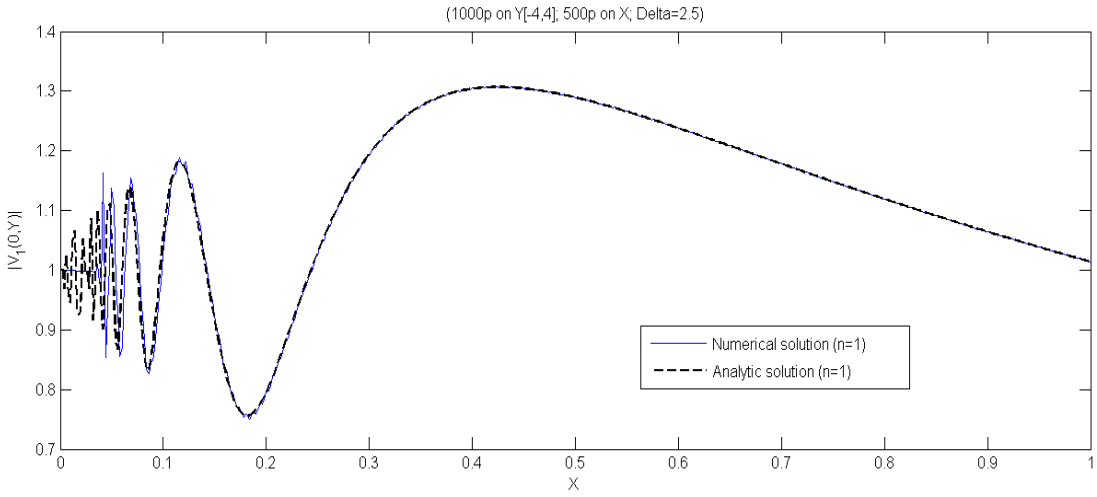

Figure 3.8: Comparison of numerical solution and analytic solution for the on-axis amplitude of the fundamental harmonic

CHAPTER 4

EXPERIMENTS

In this Chapter the specimen preparation, equipment setup, experiment procedure, and post-measurement analysis are described. Rayleigh surface waves are emitted and received by wedge transducers. In order to determine the frequency spectrum from nonlinear Rayleigh waves, the well-known fast Fourier transform is performed. This step makes it possible to normalize the amplitude of second harmonic by square of that of fundamental harmonic and such as to obtain the relative nonlinearity of the specimen material, by which the state of damage in the specimen can be determined on the basis of the theory pertaining to the nonlinear Rayleigh wave stated in Chapter 2 and Herrmann [4].

4.1 Specimen

7075-T651 Aluminum is chosen for this research. Expecting to measure the pure effect of diffraction, the undamaged specimen is used, and its measurement side (top) of surface is carefully polished by grinder and then by hand with sand papers until any visible scratch is removed. All experimental measurements are done on the same specimen. The dimension gauge of this rectangular specimen is 12 inches × 4 inches × 1 inch in length, width, and height, respectively. Figure 4.1 shows the picture of the specimen. Note that by the basic relationship of phase velocity, frequency and wavelength $\lambda = c_R/f$ and with exited frequency 2.25MHz and the approximate Rayleigh wave velocity 2927 m/s, we can obtain the estimated penetration depth about 1.3 mm. Since the penetration depth of Rayleigh waves is about 2 times of its wavelength, no reflection from the back side (bottom) of the surface of the specimen is expected. However, to reduce any reflection from the specimen's edges as much as possible, the

dimension is chosen to be laterally wide instead of a narrow dog bone shape. The following table lists essential material properties and Murnaghan constants determined in Stobbe's research [12]:

Table 4.1: Material properties of undamaged 7075-T651 aluminum

Poisson's ratio ν	0.345
Lame's constant λ $10^{10}\ N/m^2$	5.49
Lame's constant μ (shear modulus) $10^{10}\ N/m^2$	2.65
Density ρ $10^{3}\ kg/m^2$	2.700
Murnaghan constant l $10^{10}\ N/m^2$	-25.22
Murnaghan constant m $10^{10}\ N/m^2$	-32.50
Murnaghan constant n $10^{10}\ N/m^2$	-35.12

Figure 4.1: Picture of the 7075-T651 aluminum specimen

4.2 Experimental Setup

4.2.1 Transducers and Wedges

In this research, the wedge method, the most widely employed excitation method, is chosen. Piazoelectronic transducers are used to excite toneburst sinusoidal signals as plane longitudinal waves into the wedges acoustically bonded with the transducers and coupled by oil couplant. These wedges enable these input plane longitudinal waves to be converted into Rayleigh waves at the surface of the specimen. A combination of a transducer and a wedge is shown in the figure 4.2.

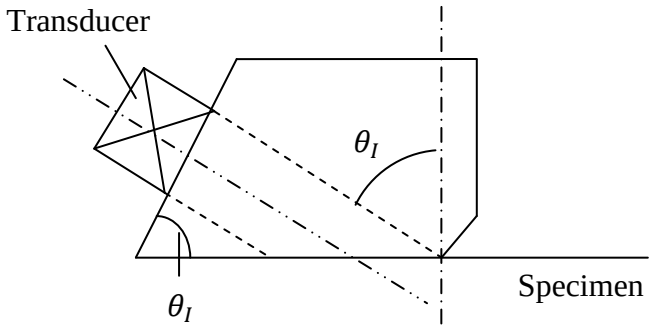

Figure 4.2: A transducer bonded with a wedge

The incident plane longitudinal wave in wedges projects into the specimen material at an angle θ_I with respect to the normal of the specimen surface, so that Rayleigh waves are generated on the theoretical basis of $sin\theta_I = c_l/c_R$, where c_R is the phase velocity of Rayleigh waves, and c_l is that of longitudinal waves. With $c_R = 2926.5\ m/s$ in the 7075-T651 aluminum specimen, which is calculated by Eq. (2.38) for approximating phase velocity of Rayleigh waves, and $c_l = 2770$ in PMMA (Plexiglas) [16], the calculated incident angle then is about $71.18°$. The optimum excitation reaches when the projection of the front edge of the wedge on to the sloping face coincides with the leading edge of the transducer [6]. Here the divergence of the longitudinal wave beam in the wedge and the displacement of the reflected beam at the wedge, because of the

solid interface between the wedge and the specimen, are neglected. In order to capture signals with frequencies as high as the second harmonic caused by material nonlinearity, the central frequency capacity of the receiver is chosen to be twice higher than that of the transmitter.

The specifications of the transmitter and receiver are tabulated as following:

Table 4.2: Specifications of transducers

	Model	Central frequency capacity	Shape	Diameter	Manufacturer
Transmitter	Panametrics X1055	2.25MHz	Circular	0.5 in.	Olympus
Receiver	Panametrics X1056	5.0MHz	Circular	0.5 in.	Olympus

4.2.2 Amplifier and Oscilloscope

A Tektronix TDS 420 oscilloscope and a high power amplifier RITEC RAM-5000 MARK IV system are employed in this research. The RITEC RAM-5000 MARK IV system is equipped with an internal trigger generator, a high power gated RF amplifier, and a cycle counter with which the width of the generated tone burst can be controlled. Since received amplitudes of the second harmonic generated by material nonlinearity is much weaker than that of the fundamental harmonic by approximately 20 times or more, high power input is important in order to get distinguishable amplitudes of the second harmonic. For this instrument, 90 percentage of maximum output voltage of RITEC amplifier is used. The following tabulates the essential specifications of RITEC RAM-5000 MARK IV system [11]:

Table 4.3: Specifications of RITEC RAM-5000 MARK IV

Frequency range for synthesizer	50 kHz - 22MHz
Nominal frequency range for gated amplifier	250kHz – 17.5 MHz
On/Off ratio of gated amplifier	>140 dB
Typical gated amplifier RMS output power	1.5kW between 0.25MHz and 7MHz

4.2.3 Connection

A set of a transmitter or a receiver consists of a piezoelectronic transducer and a wedge. First the High-power amplifier RITEC system RAM 5000 generates high amplitude input signals. The amplifier then sends these signals to the transmitter to emit real stress waves, which are finally detected by the receiver and translated back into electronic signals. These signals are sent to the oscilloscope and the PC, completing a cycle of transmitting and receiving. Since we take an average of 512 signals for every final result of measurement, the amplifier is also responsible for triggering the oscilloscope for the next signal after another in the procedure of emitting the 512 signals. The whole flow can be represented in the following figure 4.3:

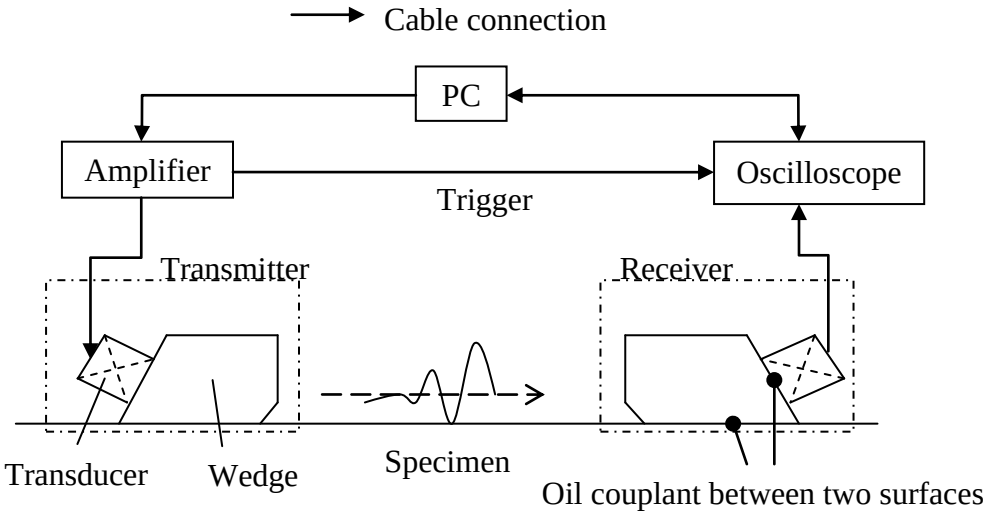

Figure 4.3: Connection for experimental setup for nonlinear ultrasonic measurements

4.2.4 Measurement Station

The measurement setup is shown in figure 4.4. The specimen is fixed with a pair of clamps to the station and together with a ruler. The purpose of the ruler is to determine the propagation distance of waves and, more importantly, to align the transmitter and the receiver. Misalignment of transmitter and the receiver would result in serious mistake since what has been measured is not the amplitude of the source on the central axis, that is, a situation similar as source asymmetry [5] [11].

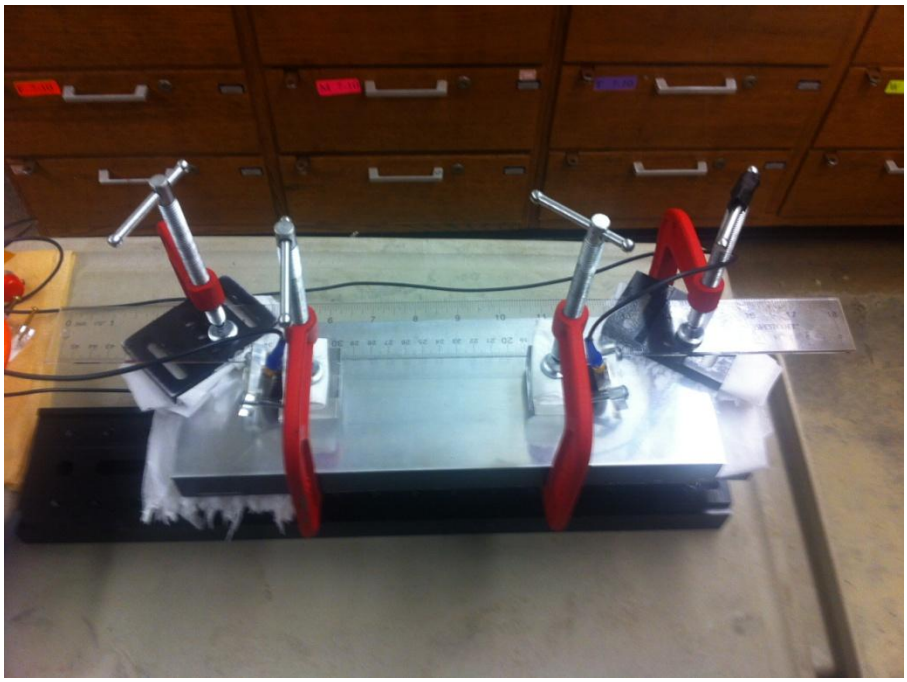

Figure 4.4: Picture of measurement station and experimental setup

4.3 Measurement Procedure

For all measurements the procedure is the same except waiting for the high power amplifier to warm up and ready. First, in order for the amplifier to warm up so that the output level is to be stable, it is necessary to wait at least 20 minutes after it is turned on [11]. The amplifier is programmed to emit tone burst sinusoidal function signals with a frequency of 2.25MHz at 90% of maximum output level. The total length of each signal

is 35 cycles in which the first few cycles are the transient state and the last few are influenced by ringing effect. Every 512 signals is generated, received with a sampling rate of 100MS/s for sufficient points in frequency analysis, and then taken an average for each measurement in order to increase signal-to-noise ratio.

As the first step, carefully clean the surface of the specimen with acetone, especially the surface within the range of propagation distance. In this research the observed range of the propagation distance is from 2.0 cm to 10.0 cm. The propagation distance is represented by the distance between the front edge of the transmitter's wedge and that of the receiver's. Couple both of the transmitter and the receiver on the specimen with one drop of oil couplant applied on the bottom of each wedge. Fix both of the transmitter and the receiver and align them along the ruler on the specimen with another pair of clamps. Be sure there is no air bubble or any small substance or particle in between the wedge and the specimen. Unlike the receiver, the transmitter will not be moved or removed during the whole progress of a series of measurements. The receiver is first placed on where the farthest measurement point in the beginning of this set of measurements, and moved to the next measurement point each time by 0.5 cm towards the transmitter. Starting from the farthest measurement point has an advantage that one is not required to clean the surface of the specimen between the transmitter and the receiver every time prior to the next measuring. After the measurement at each measurement point the receiver is completely removed from the specimen, cleaned up and reapplied a drop of oil couplant on the bottom of the wedge, and reinstalled at the next measurement point. A complete set of measurements ends at the measurement point at 2.0 cm from the transmitter.

Every result of measurements is obtained from the average of the 512 signals, recorded by the oscilloscope, sent to the computer, and saved in Excel file format.

4.4 Analysis Procedure

All analysis and signal processing are completed on the platform of MATLAB. First the measurement data is imported into MATLAB. Figure 4.5 demonstrates an example of the detected waveform of the excited 35 cycles. As mentioned in the last section, the first few cycles are in transient state, and the last few exhibit the ringing effect. For the consistency of frequency analysis results, these cycles are excluded from the target region for our analysis. The two red spots in the figure 4.5 mark the starting point and ending point. Here the first 4 cycles and the last 4 cycles are neglected, and the steady portion of cycles is filtered by windowing before fast Fourier transform (FFT) is performed. A Hann-window is chosen to be employed, since it gives better results by reducing the amplitudes of side lobes [11] [13].

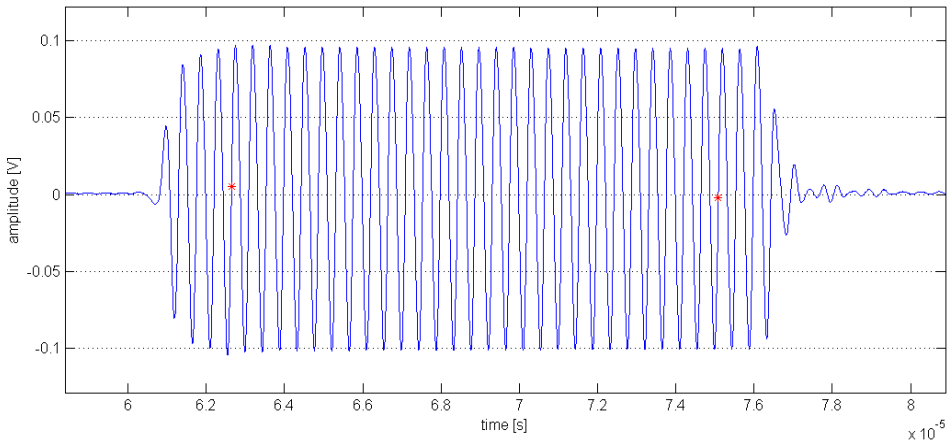

Figure 4.5: An example of time waveform of the 35 cycles for one signal

Figure 4.6 shows an example of a result of frequency spectrum analysis by FFT. Identify the uncalibrated amplitude of the fundamental harmonic and that of the second harmonic in the spectrum as A_1' and A_2', and A_1' should be as much as around 20 to 200 times A_2'. Note that since it is the vertical displacement of the fundamental and the second harmonic, u_{z1} and u_{z2}, are measured, the quantities of A_1' and A_2' are proportional to u_{z1} and u_{z2}, respectively [4]. By the Eq. (2.53) in Chapter 2, the ratio of

u_{z2} and ${u_{z1}}^2$, this is, ${u_{z2}}/{u_{z1}}^2$ is proportional to the nonlinearity β, and so is ${A_2}'/{A_1}'^2$. With a fixed the nonlinearity β, the ratio ${A_2}'/{A_1}'^2$ will only linearly change as the propagation distance varies. In Herrmann's research [4], this relationship has been proved to be an effective and promising tool for determining the level of fatigue damage at its early stage and for predicting the remaining life of materials. Figure 4.7 shows an example of the linear proportionality between the ratio of ${A_2}'/{A_1}'^2$ and propagation distances. Notice that different scales of vertical axes are in figure 4.7. The left vertical axis is for the fundamental harmonic and the right one is for the second harmonic.

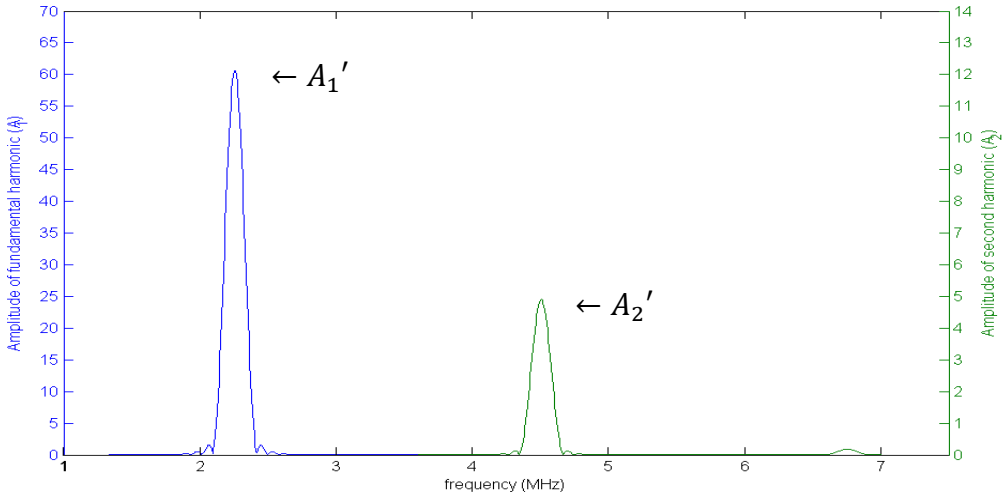

Figure 4.6: An example of a frequency spectrum and ${A_1}'$and ${A_2}'$

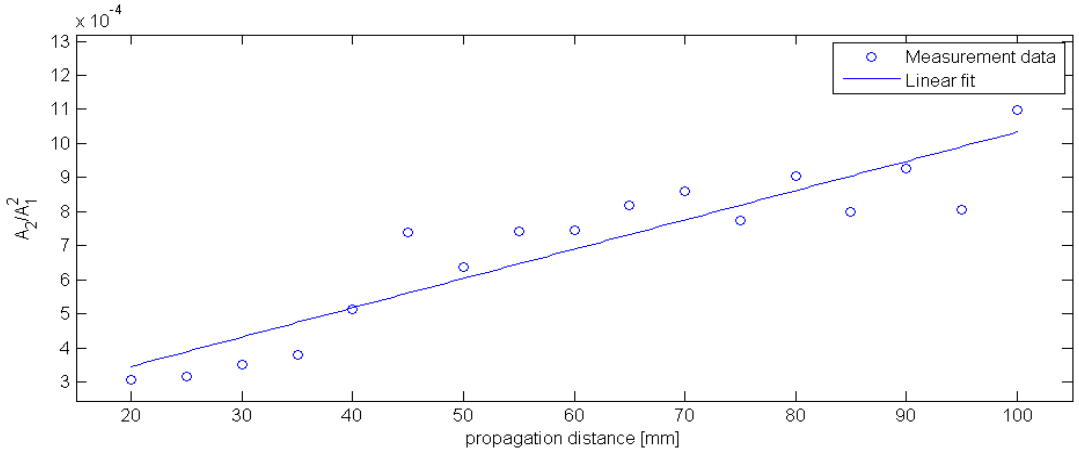

Figure 4.7: An example of normalized amplitude of second harmonic ${A_2}'/{A_1}'^2$

CHAPTER 5

EXPERIEMENTAL RESULTS AND THEIR COMPARISONS WITH THEORETICAL MODELS

Theoretical models accounting for diffraction with different source conditions have been discussed in chapter 3. With the knowledge of the last chapter, measurements of nonlinear Rayleigh waves for the amplitudes of fundamental harmonic and second harmonic and for the normalized amplitude of second harmonic are accomplished. In this chapter, theoretical models computed with three different source conditions, including a Gaussian line source, a uniform line source, and a two-dimensional Gaussian area source assembled by multiple Gaussian line sources, are compared with measurement results.

5.1 Comparison of Models and Measurements

According to Herrmann [4], each of the uncalibrated amplitude of fundamental and second harmonic, $A_1{}'$ and $A_2{}'$, is proportional to the corresponding component of displacements u_{z1} and u_{z2}, respectively, and so is $A_2{}'/A_1{}'^2$ to $u_{z2}/u_{z1}{}^2$. By following this idea, two equations are considered to establish the direct relationship between the uncalibrated quantities from FFT and the components of displacements:

$$A_1' = F_1 \times u_{z1} \tag{5.1}$$

$$A_2' = F_2 \times u_{z2} \tag{5.2}$$

where F_1 and F_2 are proportionality factors for fundamental harmonic and second harmonic, respectively. In the similar manner, the factor for the normalized second harmonic amplitude $A_2{}'/A_1{}'^2$ and the normalized displacement $u_{z2}/u_{z1}{}^2$ can be calculated by

$$\frac{A_2{}'}{A_1{}'^2} = F \times \frac{u_{z2}}{u_{z1}{}^2} \tag{5.3}$$

$$F = \frac{F_2}{{F_1}^2} \tag{5.4}$$

, where F is also a proportionality factor.

Before any comparison beginning, the components of vertical displacements u_{z1} and u_{z2} have to be calculated. The following procedure applies to all theoretical models with consideration of different source conditions in this research. A similar manner used in Hurley's work [14] is employed. Since differentiation of displacements with respect to time leads to particle velocities, we may obtain the vertical displacement amplitudes of the fundamental and second harmonic at the surface ($z = 0$) from Eq. (3.8):

$$|u_{z1}| = \frac{1}{\omega}|v_{z1}(x, y, 0, t)| = \frac{(1+\xi_l\eta)}{\omega}|v_1(x, y)| \tag{5.5}$$

$$|u_{z2}| = \frac{1}{2\omega}|v_{z2}(x, y, 0, t)| = \frac{(1+\xi_l\eta)}{2\omega}|v_2(x, y)| \tag{5.6}$$

where ω is the angular frequency of the excitation, or fundamental frequency, and v_{z1} and v_{z2} are the components of particle velocities of the fundamental and second harmonic, respectively. With the amplitudes of on-axis ($y = 0$) vertical particle velocity for the fundamental $v_{z1}(x, 0)$ and second harmonics $v_{z2}(x, 0)$ computed in chapter 3, we substitute these computation results into Eq. (5.5) and (5.6) to obtain the displacement amplitudes.

Our comparison starts from the theoretical models for a Gaussian line source and a uniform line source. Figure 5.1 shows the comparison between the measurement result, calculated from the uncalibrated amplitudes (A_1', A_2'), and the computed absolute displacements which is generated by a Gaussian line source and multiplied by factors F_1, F_2, and F for the fundamental harmonic, second harmonic, and the normalized second harmonic, respectively. In this calculation, the excited peak amplitude of particle velocity $v_0 = 0.97$m/s, $F_1 = 3 \times 10^9$, $F_2 = 2 \times 10^{10}$, the attenuation coefficients of the fundamental harmonic $\alpha_1 = 2.0$ Np/m and the assumption of $\alpha_2 = 7\alpha_1$ are chosen. In this research the nonlinearity parameter β_{11} is 0.6831, calculated with the measured

values in Stobbe's research [12]. This value of β_{11} does not agree with the range which falls between 0.13 and 0.45, calculated with literature values [14] [15]. However, 7075-T651 aluminum is contains zinc as the primary alloy element, which is different from the material of the specimens used in Hurley's work [14].

The nonlinearity parameter indicates the growth rate of the amplitude of the second harmonic, while the attenuation coefficients control the tendency of the decay of amplitude. In Figure 5.1, the theoretical model with consideration of Gaussian single line source appears to fit very well with the FFT amplitudes from measurements. The red dash line in figure 5.1(c) is the linear fitting for the FFT amplitudes of the normalized second harmonic from measurements. The theoretical model of the normalized second harmonic, which is calculated with the models of the fundamental and second harmonic by the ratio $\frac{u_{z2}}{{u_{z1}}^2}$, shows a good match with the linear fitting at the propagation distance between about 50 mm to 80 mm, where the measurement less influenced by diffraction and thus more reliable. This good match shows a reliable agreement between the calculated amplitude of normalized second harmonic and the linear fitting, and thus it is also reliable to apply the theoretical models to predicting the amplitudes of the fundamental harmonic, the second harmonic, and the normalized second harmonic in the nearfield with the method proposed in this research.

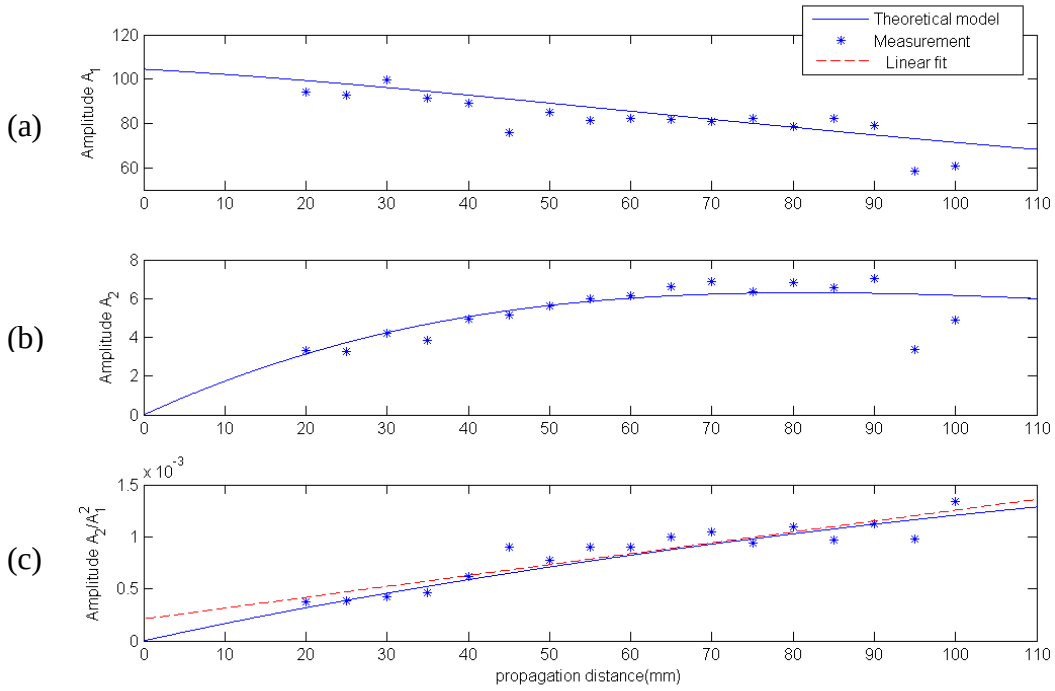

Figure 5.1: The comparison of FFT amplitudes and theoretical models of (a) the fundamental harmonic, (b) the second harmonic, and (c) the normalized second harmonic excited by Gaussian line source

As discussed in chapter 2 and in the work of Herrmann's [4] and Walker's research [11][19], the variation of the slope of the linear fitting for the amplitudes of the normalized second harmonic can be considered as a promising tool for determining the level of plastic damages at its early stage on the theoretical basis of the relationship between the material nonlinearity and the amplitude of the normalized second harmonic. With the method proposed in this research, one may predict the slope of linear fitting resulted from the amplitude of the normalized second harmonic by simply conducting measurements in a small propagation distance range, or may also reduce the measurement points required for determining the slope.

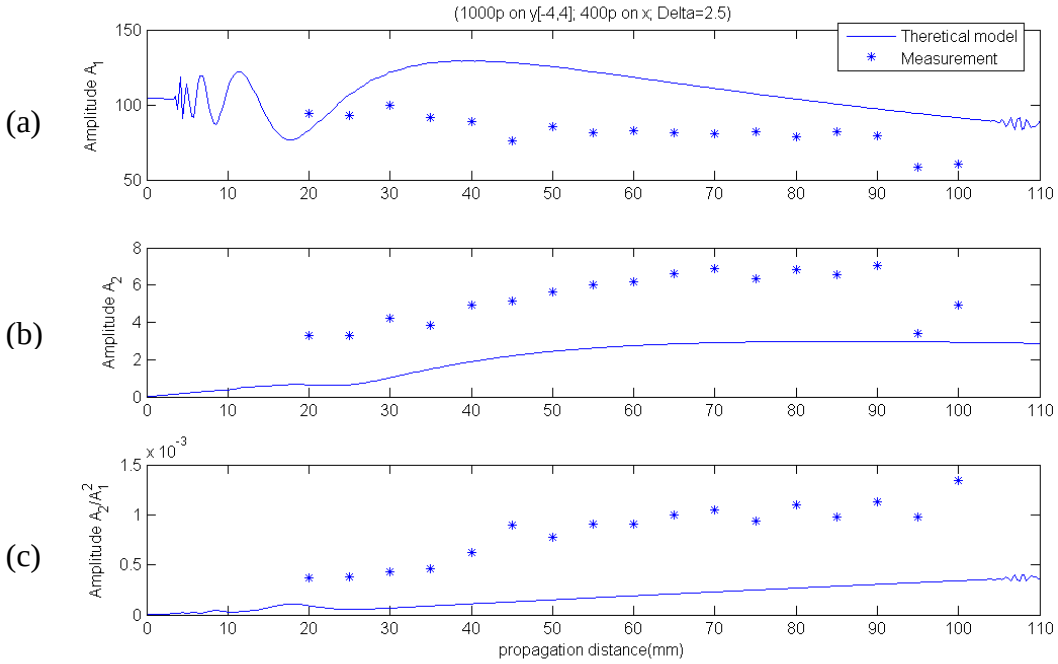

(a)

(b)

(c)

Figure 5.2: The comparison of FFT amplitudes and theoretical models of (a) the fundamental harmonic, (b) the second harmonic, and (c) the normalized second harmonic excited by uniform line source

Figure 5.2 shows the comparison of the measurement result and the theoretical model calculated with uniform single line source. All parameters, including attenuation coefficients and factors F, F_1, and F_2, are chosen the same with those used in the last comparison. The theoretical model of uniform line sources is computed with the Eq. (3.21) within the modification of variables with normalized for cylindrical spreading beams. For the computation of the model, parameters used in chapter 3 continue to be applied here, including 1000 computation points $\bar{Y}$ direction, the boundaries on $\bar{Y} = -4 \; and \; 4$, and $\delta = 2.5$, but 400 calculation points between $\bar{X} = 0$ and 1.1 are used. Lowering resolution in $\bar{X}$ direction only causes subtle differences on calculation results but greatly reduces computation time. Apparently, the model with consideration of the uniform line source condition does not fit the measurement result as good as the last model does. Even though the two models have nearly the same starting amplitude of the

fundamental harmonic, the amplitude of the second harmonic calculated by the model for uniform line source still deviates from that calculated by the model for Gaussian line source and from the measurement results. The comparison of the two theoretical models is provided in figure 5.3.

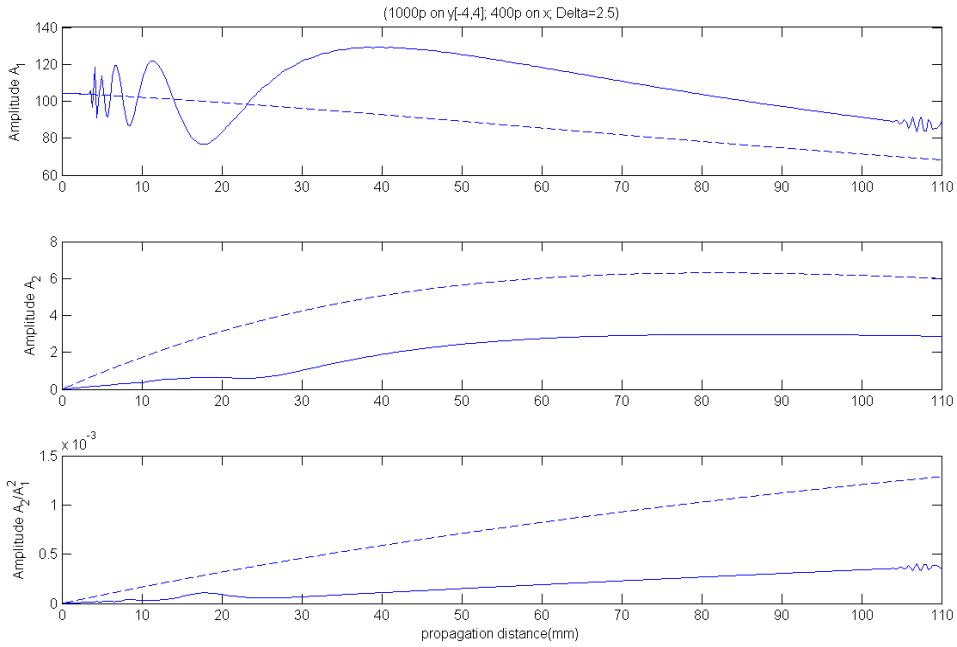

Figure 5.3: The comparison of the theoretical models for uniform line source (solid) and for Gaussian line source (dashed)

5.2 Comparison of Models for a Gaussian Area Source and Measurements

Since the shape of the transducers is circular, the investigation in this section is given to the comparison of the measurement results and a theoretical model modified from the original model of Gaussian line source.

Consider an area source which is assembled by multiple Gaussian line sources. This area source may be assumed to be in a shape of ellipse, since the projection of the circular transducer on the specimen at an incident angle is no longer circular but elliptical. The basic function of ellipse $\left(\frac{x}{a}\right)^2 + \left(\frac{y}{b}\right)^2 = 1$ is introduced as a shape function with

which Gaussian line sources are assembled, where a is the diameter of the circular transducer, $b = \frac{a}{\cos\theta_I}$ is the length projected from the diameter of the circular transducer to the specimen surface in the x direction, and $\theta_I = 71.18°$ is the incident angle calculated in the chapter 4. Figure 5.4 illustrates this assembled area source. This projected ellipse splits into Gaussian line sources laying along the y direction. The displacement generated by this area source is calculated by assembling the displacements excited by each of those Gaussian line sources by separately adding the real part and the imaginary part of those displacements. The number of the line sources depends on the resolution on x direction used when computing the single line source, that is, the distance between two line sources is equal to the resolution on x direction. The lengths of those line sources vary with x direction within the ellipse. The peak excitation amplitude v_0 of each line source also varies with obeying to the source function of the Gaussian line source in the chapter 3 for x direction (replace y with x in the source function of the Gaussian line source). The center of the elliptical area source locates at the origin of x-y plane.

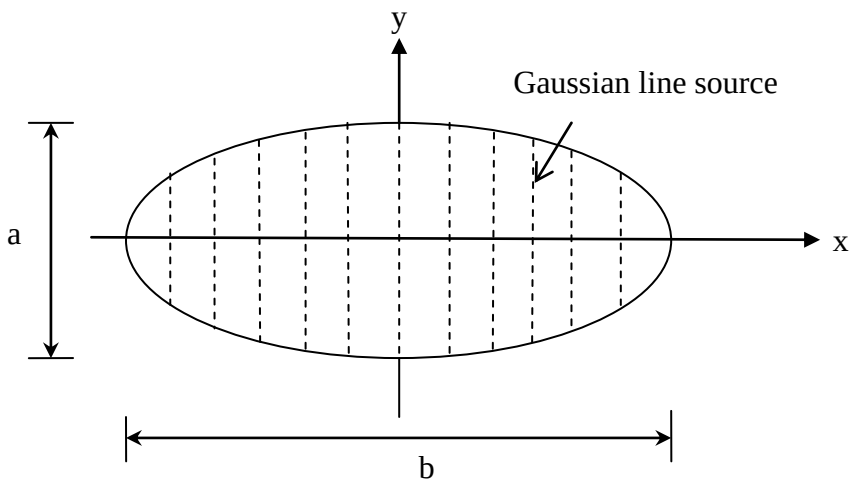

Figure 5.4: The elliptical area source assembled by multiple Gaussian line sources

The same manner and parameter values in the last section except for the attenuation coefficients and the proportionality factors F_1, F_2, and F continue to be employed in the calculation for this model. Adjusting proportionality factors only evenly changes the amplitudes of the theoretical curves for each of their own harmonic. In this case, the model for the area source is first computed with $F_1 = 1.5 \times 10^7$, $F_2 = 4.5 \times 10^7$, $\alpha_1 = 0.6$, and $\alpha_2 = 2.5\alpha_1$.

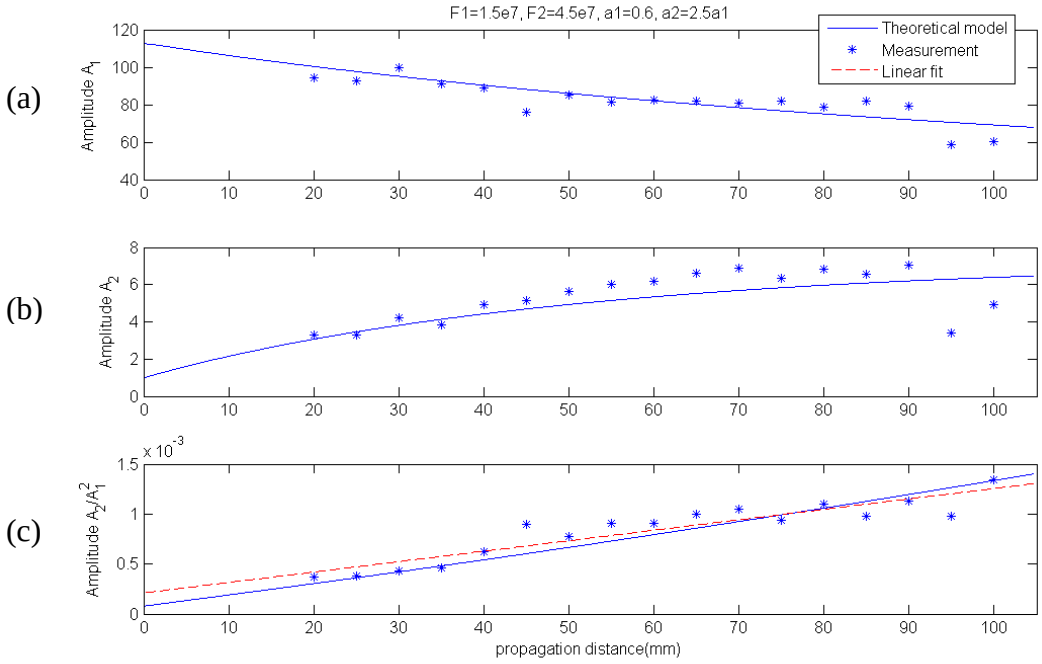

Figure 5.5: The comparison of FFT amplitudes and theoretical models of (a) the fundamental harmonic, (b) the second harmonic, and (c) the normalized second harmonic exited by assembled Gaussian area source

Figure 5.5 demonstrates the result of computation as well as the FFT amplitudes resulted from measurements. Again, the red dashed line is the linear fitting of the amplitudes of the normalized second harmonic. The theoretical model of the second harmonic does not begin from zero because it is where the center of the source locates at. With parameters carefully chosen, this model, though assembled linearly, can also fit the measurement results well. Since the attenuation coefficient of the second harmonic has a

limit of no less than or equal to $2\alpha_1$ in Eq. (3.16), the rate of the decay of the second harmonic in figure 5.5(b) has almost reached its minimum. For the normalized second harmonic, there is still a small region between propagation distances at about 70 mm to 80 mm where the slope calculated by theoretical models meet with the linear fitting computed from measurements; however, outside of this region the theoretical model immediately begins to deviate from the linear fitting, unlike the model with Gaussian line source which exhibits not only agreement in a longer region but also fit closely to the trend of the measurement results at distances both near and far from the source. As a conclusion, the model with Gaussian line source also predicts measurement results better than the model with assembled area source does. This conclusion corresponds to a statement in Herrmann's work [4] that a wedge transducer can be considered as an effective line source if the front edge of the ultrasonic beam in this wedge coincides with the front edge of the wedge.

CHAPTER 6

CONCLUSION

In this research, a method is proposed to relate the uncalibrated nonlinearity parameters in FFT frequency spectrum from measurements to the theoretical ones. The normalized amplitude of second harmonic computed by different theoretical models is compared with that calculated from measurement results.

Theoretical models of nonlinear Rayleigh waves with the diffraction effect accounted for and with different excitation source are individually studied, and those models are also implemented by either existing analytic solutions or by solving differential equation systems numerically. The analytic solution for the amplitudes of particle velocity exited by Gaussian line source is first implemented. Next the quasilinear partial differential equation system with uniform line source condition is solved numerically. The model solved by the original equation system gives only a rough trend of the curve without details in the nearfield, yet greatly consumes time for computation. For computation efficiency and more details in the nearfield, this partial differential equation system is first improved by normalizing variables and then modified by transforming the rectangular coordinate into a coordinate for cylindrically spreading beams. The first modified differential equations, though saving much more time than the original equations on computation and providing details in the nearfield of the resulting curve, still encounter a problem of revealing trembles on the solved model. The second modified equations effectively reduce computation time and meanwhile provide an even better result by showing more details in the nearfield, removing trembles on the curve as long as right parameters are chosen, and matching closely with the analytic solution.

With proper parameters chosen, the propose method in this research is able to successfully connect the displacement calculated from the theoretical models to the

uncalibrated amplitudes of fast Fourier transform from measurement. This method provides a feasible way to determine the normalized amplitude of the second harmonic in a small propagation distance by predicting with theoretical models, and thus improves the technique for charactering damage at its early stage with use of nonlinear Rayleigh waves generated by the wedge method. The applicability of different theoretical models to predict the result of measurements is compared in chapter 5. The model with Gaussian line source condition has better ability to fit the measurement results.

Although the proposed method for predicting measurement results with theoretical models shows a promise, the procedure of choosing parameters, including attenuation coefficients and multiplying factors F_1, F_2, and F for matching the theoretical models and FFT amplitudes resulted from measurements, may require a great deal of work and time. Extension research concentration may concentrate finding a direct connection between the voltages measured with the transducer and the absolute displacement amplitudes in order to develop a method for directly determining these multiplying factors by calculation. In addition, since the model for Gaussian area source is assembled linearly, the validity of this model should be further investigated and verified. Furthermore, the errors between measurement results and theoretical models with different source conditions should be determined quantitatively in order to compare more precisely the validities of these models. These extension research topics may be constructive to the improvement of the technique for characterizing the damage level of material by using nonlinear Rayleigh waves, since they may lay a solid foundation for performing this technique in short propagation distance and on small structural elements or parts.

REFERENCES

[1] Achenbach, J. D., "Propagation in Elastic Solids," North-Holland Pub. Co., New York, (1975).

[2] Graff, K. F., "Wave Motion in Elastic Solids," originally by Ohio State University Press, (1975), abridged edition by Dover Pub., (1991).

[3] Hamilton, M. F. and Blackstock, D. T., "Nonlinear Acoustics," Academic Press, (1998).

[4] Herrmann, J., Kim, J.-Y., Jacobs, L. J., Qu, J. M., Littles, J. W., and Savage, M. F., "Assessment of Material Damage in a Nickel-base Superalloy Using Nonlinear Rayleigh Surface Waves," Journal of Applied Physics, vol. 99, no. 12, (2006).

[5] Zabolotskaya, E. A., "Nonlinear Propagation of Plane and Circular Rayleigh Waves in Isotropic Solids," J. Acoust. Soc. Am., Vol. 91, no. 5, p. 2569-2575, (1992).

[6] Viktorov, I., "Rayleigh and Lamb Waves," Physical Theory and Applications, Plenum Press New York, (1967).

[7] Thompson, R. B., "Harmonic Generation of Longitudinal Elastic Waves," J. Acoust. Soc. Am., Vol. 62, no.1, p.33-37, (1977).

[8] Baker, B. B. and Copson, E. T., "The Mathematical Theory of Huygens' Principle," Book, 2nd edition, Oxford University Press, (1950).

[9] Shull, D. J., Kim, E. E., Hamilton, M. F. and Zabolotskaya, E. A., "Diffraction Effects in Nonlinear Rayleigh Wave Beams," J. Acoust. Soc. Am., Vol. 97, no. 4, p. 2126-2137, (1995).

[10] Shull, D. J., Hamilton, M. F., Il'insky, Yu. A., and Zabolotskaya, E. A., "Harmonic Generation in Plane and Cylindrical Nonlinear Rayleigh Waves," J. Acoust. Soc. Am., Vol. 94, no. 1, p. 418-426, (1993).

[11] Walker, S. V., "Characterization of Fatigue Damage in A36 Steel Specimens Using Nonlinear Rayleigh Surface Waves," Master's thesis, Georgia Institute of Technology, (2001).

[12] Stobbe, D. M., "Acoustoelasticity in 7075-T651 Aluminum and Dependence of Third Order Elastic Constants on Fatigue Damage," Master's thesis, Georgia Institute of Technology, (2005).

[13] Oppenheim, A., Schafer, R., and Buck, J., "Discrete-time Signal Processing," Book, Prentice-Hall signal processing series, Prentice Hall, (1999).

[14] Hurley, D. C., "Nonlinear Propagation of Narrow-band Rayleigh Waves Excited by a Comb Transducer," J. Acoust. Soc. Am., Vol. 106, no. 4, Pt. 1, p.1782-1788, (1999).

[15] Raju, V. K., Reddy, P. J., "Third-order Elastic Moduli of Polycrystalline Al-Mg and Al-Cu Alloys", Journal of Physics D, Applied Physics, Vol. 14, p65-70, (Jan. 1981).

[16] Henckel, A., Takayama, K., Gronig, H., "Study of Mach Reflection in PMMA Plates," International Symposium on Shock Waves and Shock Tubes (15th:1985: Berkeley. Calif.), Stanford University Press, p. 869 – 876, (1986).

[17] Liu, M. H., Kim, J.-Y., Jacobs, L. J., Qu, J. M., "Experimental Study of Nonlinear Rayleigh Wave Propagation in Shot-peened Aluminum Plates---Feasibility of Measuring Residual Stress," NDT & E International, Vol. 44, p. 67-74, (2011).

[18] Anon., "Wave Diffraction in the Manner of Huygens and Fresnel", http://upload.wikimedia.org/wikipedia/commons/6/60/Refraction_on_an_aperture_-_Huygens-Fresnel_principle.svg

[19] Walker, S. V., Kim, J.-Y., Qu, J. M., Jacobs, L. J., "Fatigue Damage Evaluation in A36 Steel Using Nonlinear Rayleigh Surface Waves," NDT & E International, Vol. 48, p. 10-15, (2012).